

Development of a scalable high-order conservative nonhydrostatic model by using multi-moment finite volume method

Xingliang Li¹, Chungang Chen², Xueshun Shen¹ and Feng Xiao³

1 Numerical Weather Prediction Centre, China Meteorological Administration, Beijing 100081, China

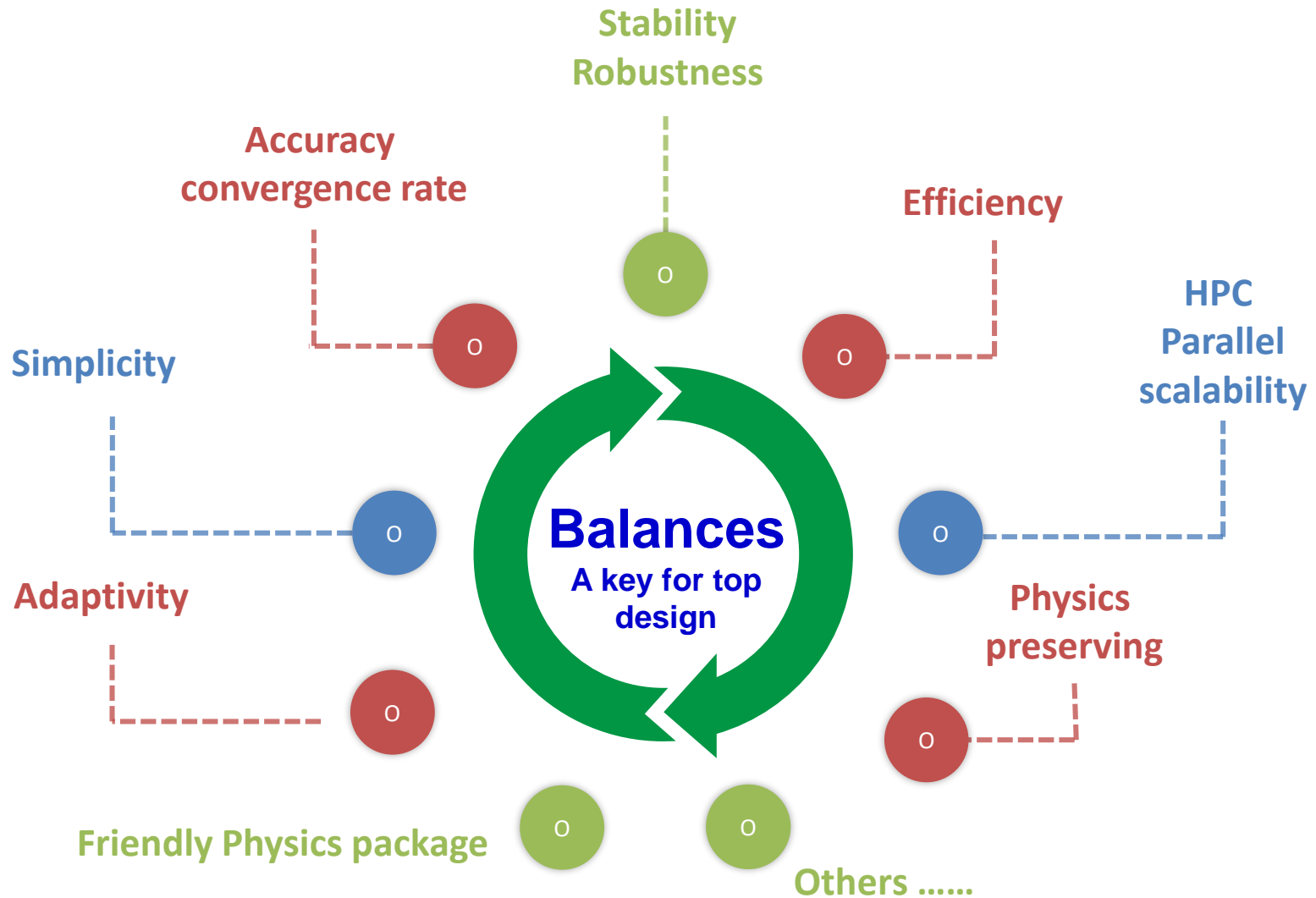
2 State Key Laboratory for Strength and Vibration of Mechanical Structures & School of Aerospace , Xi'an Jiaotong University, Xi'an, Shaanxi 710049, China

3 Department of Mechanical Engineering, Tokyo Institute of Technology, Yokohama 226-8502, Japan


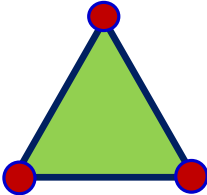
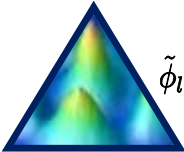
ECMWF Annual Seminar
09/18/2020



The balances in designing numerical formulations for any atmospheric model



Conservative numerical solvers for CFD

Method	DOFs(Unknowns)	Features
Conventional FVM	 $\bar{\phi}_i(t) = \frac{1}{ V_i } \int_{V_i} \phi(X, t) dV$	Simplicity, conservation, low accuracy (2 nd O), not easy for high order
Multi-moment FVM	 $\bar{\phi}_i(t) = \frac{1}{ V_i } \int_{V_i} \phi(X, t) dV$ $\phi_{ij}(t) = \phi(X_{ij}, t)$	A tradeoff balanced between accuracy & Complexity
Spectral/hp element with flux concept, DG, SE	 $\tilde{\phi}_l(t) = \left\langle \left(\sum_{k=1}^K \tilde{\phi}_k(t) \tilde{\psi}_k(X) \right), \tilde{\psi}_l(X) \right\rangle$	Compact stencil, High accuracy, Complexity

Requirement of the numerical model

Conservation

(Local/global)

Accuracy

(High-order)

Scalability

(Many-cores)

Grid robustness

(Mesh-adaptivity)



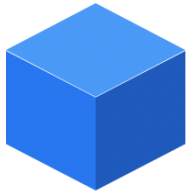
- The **multi-moment finite volume method** has the potential to satisfy the above requirements.

MM-FV: Multi-**M**oment **F**inite **V**olume method

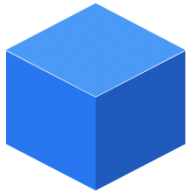
Outlines



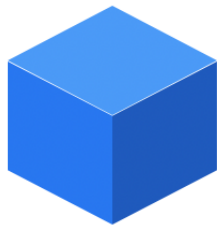
Numerical Formulations



MM-FV DynCore on cubed sphere



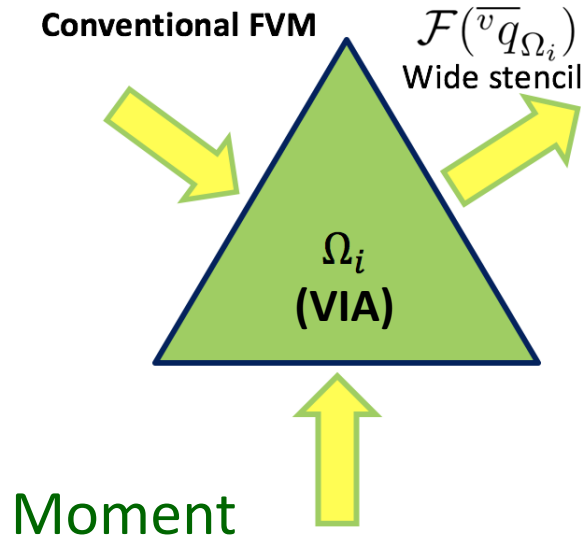
Summary



Numerical Formulations

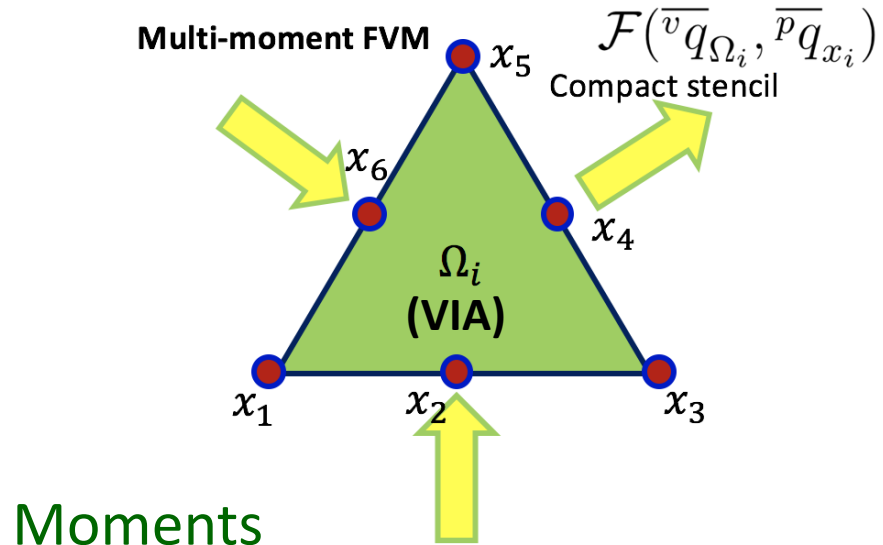
Multi-moment finite volume method

“Derivation: Form I” (li & Xiao, JCP, 2009)



Volume integrated average(VIA)

$$\overline{v}q_{V_i}(t) = \frac{1}{|V_i|} \int_{V_i} q(x, t) dV$$



<p>Volume integrated average (VIA)</p> $\overline{v}q_{V_i}(t) = \frac{1}{ V_i } \int_{V_i} q(x, t) dV$	Point value (PV)
	Derivative value (DV)
	$\overline{p}q_{x_j}(t) = q(x_j, t)$ $\overline{D_k}q_{x_j}(t) = \frac{\partial^{[k]}}{\partial x^{[k]}} q(x_j, t)$

Multi-moment method uses two or more kinds of moments

A multi-moment FV method distinguishes, memorizes and updates all of the moments.

Multi-moment finite volume scheme

MCV scheme is an extension of finite volume method with better efficiency and flexibility

Consider the conservation law

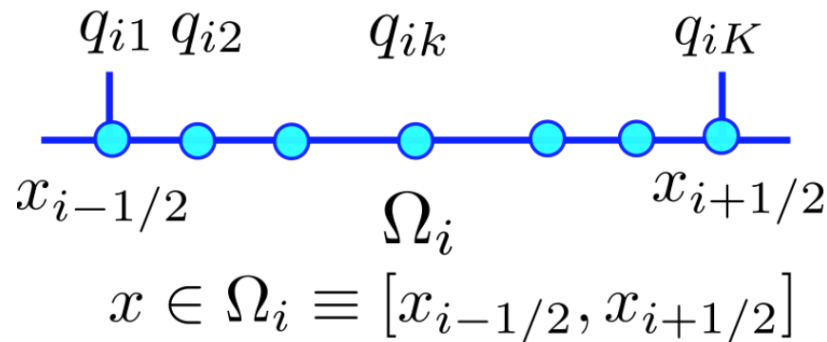
$$\frac{\partial q}{\partial t} = - \frac{\partial f(q)}{\partial x} \quad (1)$$

“Derivation: Form II”

*multi-moment constrained
flux reconstruction*

(Xiao et al., AMM, 2013)

Define the solution points at x_{ik}



$$\hat{f}_i(x)$$

Local reconstruction

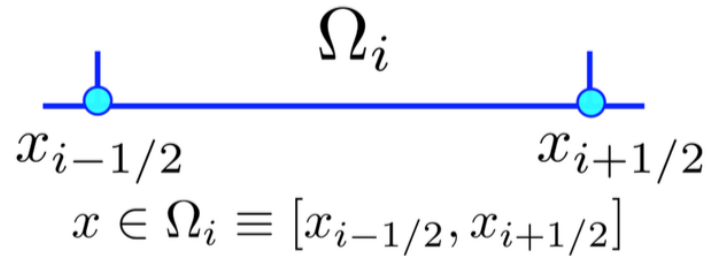
The point-wise semi-discretised equations at solution points x_{ik} read

$$\frac{dq_{ik}}{dt} = - \left[\frac{d\hat{f}_i(x)}{dx} \right]_{ik} = - \left(\frac{d\xi}{dx} \right)_i \left[\frac{d\hat{f}_i(\xi)}{d\xi} \right]_{ik}, \quad k = 1, 2, \dots, K.$$

Local coordinate $\xi \iff x$ global coordinate

Numerical conservation

Integrate the equation (1) over the interval $[x_{i-1/2}, x_{i+1/2}]$



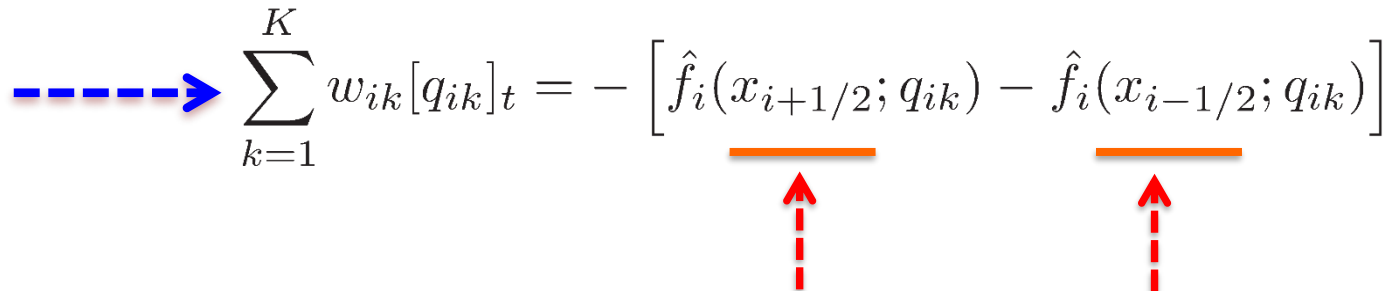
A horizontal blue line segment represents the interval Ω_i . At each end of the segment, there is a small vertical blue tick mark and a solid blue circle. Below the left circle is the label $x_{i-1/2}$ and below the right circle is the label $x_{i+1/2}$. Above the center of the segment is the label Ω_i . Below the segment, centered, is the equation $x \in \Omega_i \equiv [x_{i-1/2}, x_{i+1/2}]$.

$$\Omega_i$$

$$x_{i-1/2} \qquad x_{i+1/2}$$

$$x \in \Omega_i \equiv [x_{i-1/2}, x_{i+1/2}]$$

$$\int_{x_{i-1/2}}^{x_{i+1/2}} \frac{\partial q(x, t)}{\partial t} dx = - \int_{x_{i-1/2}}^{x_{i+1/2}} \frac{\partial \hat{f}(x; q_{ik})}{\partial x} dx$$



A blue dashed arrow points from the left towards the summation term of the equation. The equation is $\sum_{k=1}^K w_{ik} [q_{ik}]_t = - \left[\hat{f}_i(x_{i+1/2}; q_{ik}) - \hat{f}_i(x_{i-1/2}; q_{ik}) \right]$. Below the first term in the brackets, $\hat{f}_i(x_{i+1/2}; q_{ik})$, there is a solid orange horizontal line with a red dashed arrow pointing up to it. Similarly, below the second term, $\hat{f}_i(x_{i-1/2}; q_{ik})$, there is a solid orange horizontal line with a red dashed arrow pointing up to it.

$$\sum_{k=1}^K w_{ik} [q_{ik}]_t = - \left[\hat{f}_i(x_{i+1/2}; q_{ik}) - \hat{f}_i(x_{i-1/2}; q_{ik}) \right]$$

Numerically conserved while the flux function is continuous at the cell boundary

$$\hat{f}_i(x_{i-1/2}; q_{ik}) = f_{i-1/2}^{\mathcal{B}}$$

Multi-moment constrained collocation scheme

MCV scheme is an extension of finite volume method with better efficiency and flexibility

Consider the conservation law

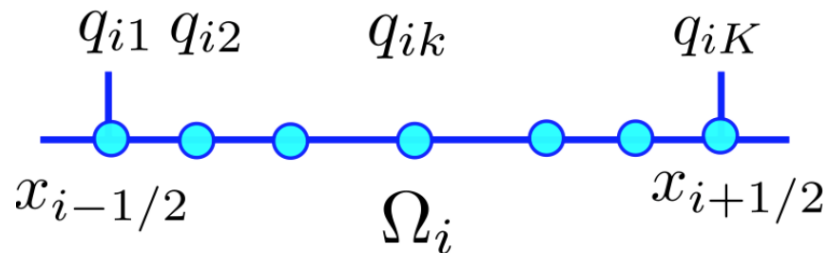
$$\frac{\partial q}{\partial t} = - \frac{\partial f(q)}{\partial x} \quad (1)$$

“Derivation: Form II”

*multi-moment constrained
flux reconstruction*

(Xiao et al., AMM, 2013)

Define the solution points at x_{ik}



$$x \in \Omega_i \equiv [x_{i-1/2}, x_{i+1/2}]$$

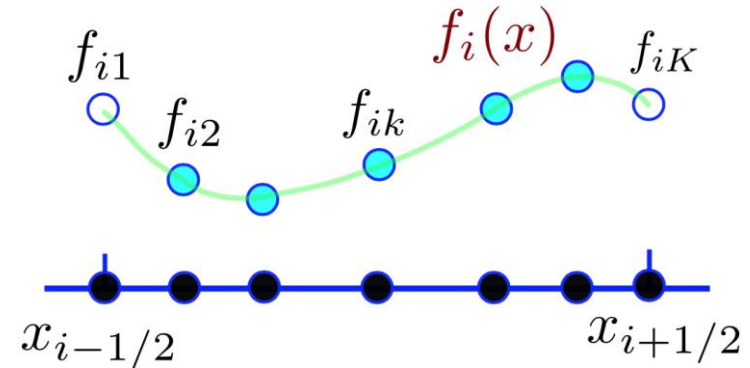
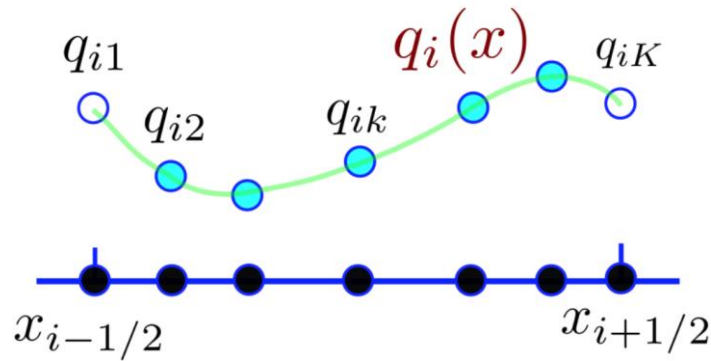
The point-wise semi-discretised equations at solution points x_{ik} read

$$\frac{dq_{ik}}{dt} = - \left[\frac{d\hat{f}_i(x)}{dx} \right]_{ik} = - \left(\frac{d\xi}{dx} \right)_i \left[\frac{d\hat{f}_i(\xi)}{d\xi} \right]_{ik}, \quad k = 1, 2, \dots, K.$$

Local coordinate $\xi \iff x$ global coordinate

$$\hat{f}_i(x) \quad ?$$

Primary flux reconstruction



Given the variable q_{ik} at the solution point x_{ik}

The cell-wise Lagrange interpolation of polynomial of degree $K - 1$ for $q_i(x)$

$$q_i(x) = \sum_{k=1}^{K-1} q_{ik} \phi_{ik}(x)$$

and for the flux function $f_i(x)$

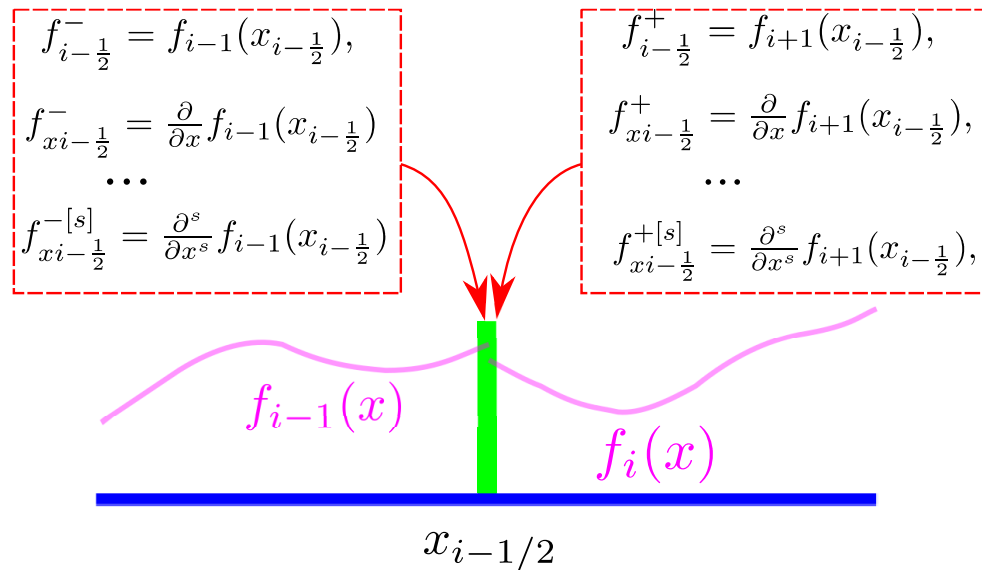
$$f_i(x) = \sum_{k=1}^{K-1} f_{ik} \phi_{ik}(x)$$

The Lagrange base function $\phi_{ik}(x)$ reads

$$\phi_{ik}(x) = \prod_{j=1, j \neq k}^K \frac{x - x_{ij}}{x_{ij} - x_{ik}}$$

Note: Primary function can not be directly utilized

The numerical flux of cell boundary by the primary function



$$f_{i-\frac{1}{2}}^{\mathcal{B}} = \text{Riemann}(f_{i-\frac{1}{2}}^-, f_{i-\frac{1}{2}}^+)$$

$$f_{xi-\frac{1}{2}}^{\mathcal{B}[s]} = \text{Riemann}(f_{xi-\frac{1}{2}}^{[s]-}, f_{xi-\frac{1}{2}}^{[s]+})$$

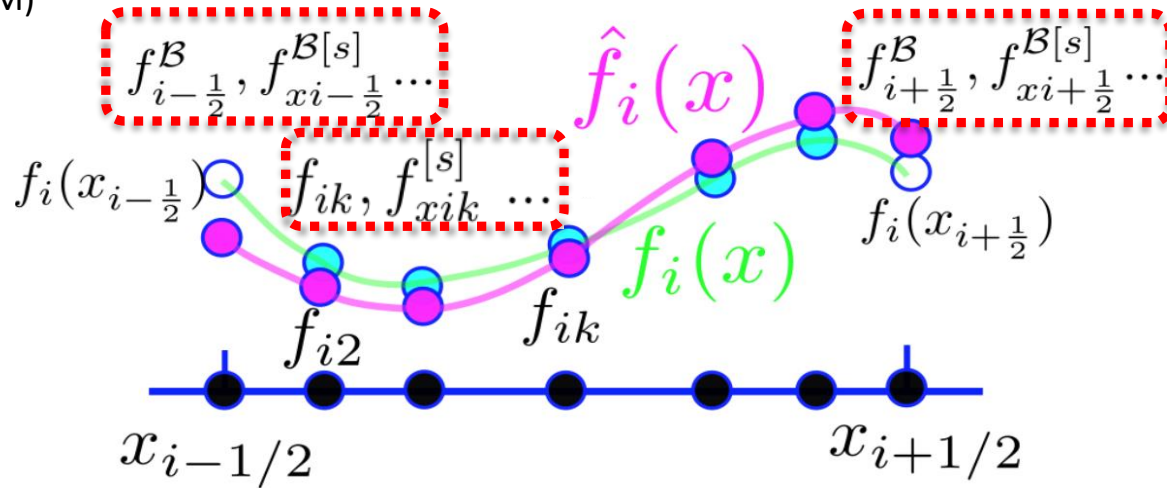
The approximate Riemann solvers such as local Lax–Friedrich (LLF), Roe are used for simplicity

Kolgan(70s); Ben-Artzi ,Li, Falcovitz(84, 89,06,07.09), Toro et al. [ADER](02,...)

The preparation for construction of the modified flux function

The Herimte type modified flux reconstruction

(Xiao et al., 2013, AMM)



More informations are given such as

- ✧ point value (PV) of solution point,
- ✧ the derivative values (DV) of solution point,
- ✧ the cell boundary flux and its derivative.

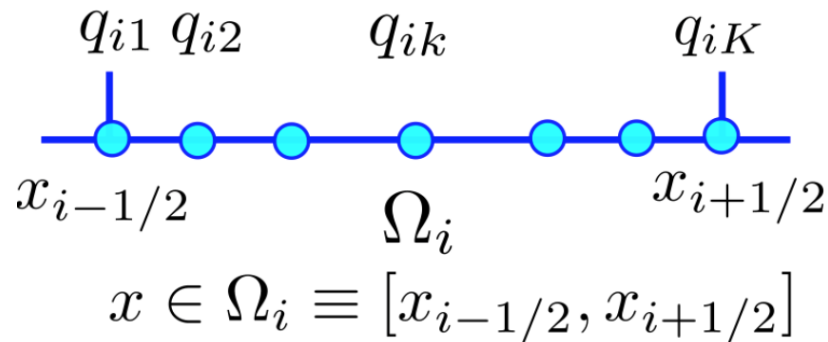
The modified flux function

$$\hat{f}_i(x) = \text{Reconstruction}(f_{i-\frac{1}{2}}^{\mathcal{B}}, f_{xi-\frac{1}{2}}^{\mathcal{B}[s]}, f_{ik}, f_{xik}^{[s]}, \dots)$$

Last step: evolution equation of solution point

$$\hat{f}_i(x) = \text{Reconstruction}(f_{i-\frac{1}{2}}^{\mathcal{B}}, f_{xi-\frac{1}{2}}^{\mathcal{B}[s]}, f_{ik}, f_{xik}^{[s]}, \dots) \quad (\text{now known})$$

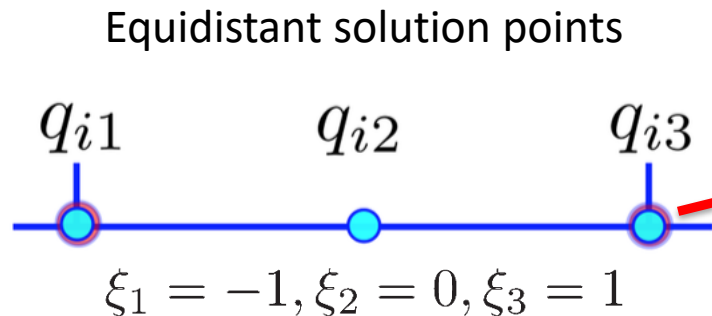
Directly differentiate the modified reconstructed function at the solution point



$$\frac{dq_{ik}}{dt} = - \left[\frac{d\hat{f}_i(x)}{dx} \right]_{ik} = - \left(\frac{d\xi}{dx} \right)_i \left[\frac{d\hat{f}_i(\xi)}{d\xi} \right]_{ik}, \quad k = 1, 2, \dots, K.$$

Example: Multi-moment constrained finite volume method (MCV3) 3rd

$$\left\{ \begin{array}{l} \hat{f}_i(-1) = f_i^{\mathcal{B}}(-1) \\ \hat{f}_i(1) = f_i^{\mathcal{B}}(1) \\ \hat{f}_{\xi i}^{[1]}(-1) = f_{\xi i}^{\mathcal{B}}(-1) \\ \hat{f}_{\xi i}^{[1]}(1) = f_{\xi i}^{\mathcal{B}}(1) \end{array} \right.$$



Impose Hermite constraints on the boundary

Evolution equations to update the nodal values

Reconstruction of the modified flux function of degree 3

$$\frac{dq_{ik}}{dt} = -\hat{f}_{\xi i}(\xi_k) = -\hat{f}_{\xi ik}, k = 1, 2, 3$$

$$\hat{f}_i(\xi)$$

$$\left\{ \begin{array}{l} \hat{f}_{\xi i1} = f_{\xi i}^{\mathcal{B}}(-1), \\ \hat{f}_{\xi i2} = \frac{1}{4}(3f_i^{\mathcal{B}}(1) - 3f_i^{\mathcal{B}}(-1) - f_{\xi i}^{\mathcal{B}}(-1) - f_{\xi i}^{\mathcal{B}}(1)), \\ \hat{f}_{\xi i3} = f_{\xi i}^{\mathcal{B}}(1), \end{array} \right.$$

Numerical conservation

$$\int_{-1}^1 \hat{f}_{\xi i}(\xi) d\xi = \sum_{k=1}^3 (w_k \hat{f}_{\xi ik}) = \frac{1}{3} \hat{f}_{\xi i1} + \frac{4}{3} \hat{f}_{\xi i2} + \frac{1}{3} \hat{f}_{\xi i3} = f_i^{\mathcal{B}}(1) - f_i^{\mathcal{B}}(-1)$$

Fourier analysis (Xiao et al., 2013, AMM)

Consider the linear advection equation $\frac{\partial q}{\partial t} + \frac{\partial q}{\partial x} = 0$,
the reconstructed flux function can be expressed in terms of the values
at solution points within $[x_{i-\frac{3}{2}}, x_{i-\frac{1}{2}}]$ and $[x_{i-\frac{1}{2}}, x_{i+\frac{1}{2}}]$

$$\hat{f}_x(x_{ik}) = \begin{pmatrix} s_{i1k} \\ s_{i2k} \\ \dots \\ s_{iKk} \end{pmatrix}^T \times \begin{pmatrix} q_{i1} \\ q_{i2} \\ \dots \\ q_{iK} \end{pmatrix}$$

Use a wave solution $q(x, t) = e^{I\omega(x-t)}$
 $q_{ik} = e^{I\omega(i+\xi_k/2)}$ and $q_{i-1k} = e^{I\omega} q_{ik}$

$$\hat{f}_x(x_{ik}) = \begin{pmatrix} c_{i-11k} \\ c_{i-12k} \\ \dots \\ c_{i-1Kk} \\ c_{i1k} \\ c_{i2k} \\ \dots \\ c_{iKk} \end{pmatrix}^T \times \begin{pmatrix} q_{i-11} \\ q_{i-12} \\ \dots \\ q_{i-1K} \\ q_{i1} \\ q_{i2} \\ \dots \\ q_{iK} \end{pmatrix}$$

$$\begin{cases} \frac{dq_{i1}}{dt} = -\hat{f}_x(x_{i1}), \\ \frac{dq_{i2}}{dt} = -\hat{f}_x(x_{i2}), \\ \dots\dots\dots \\ \frac{dq_{iK}}{dt} = -\hat{f}_x(x_{iK}), \end{cases}$$

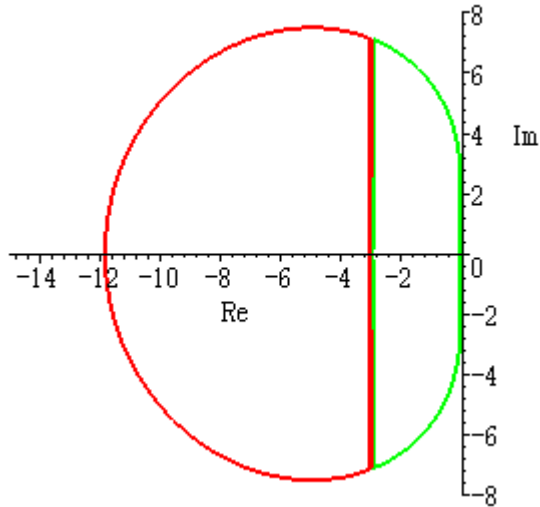
We have the vector form

$$\frac{d\mathbf{q}_i}{dt} = \mathbf{S}\mathbf{q}_i$$

where \mathbf{S} is the amplification matrix.

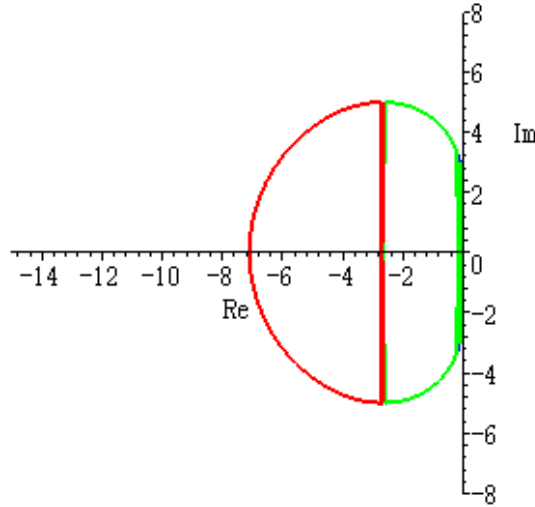
The Eigenvalue & Spectrum of Space-discretization

Discontinuous Galerkin



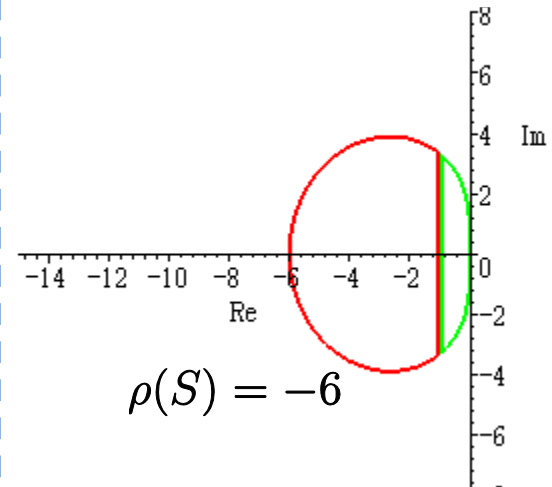
$$\rho(S) = -11.84236$$

Spectral collocation



$$\rho(S) = -7.10005$$

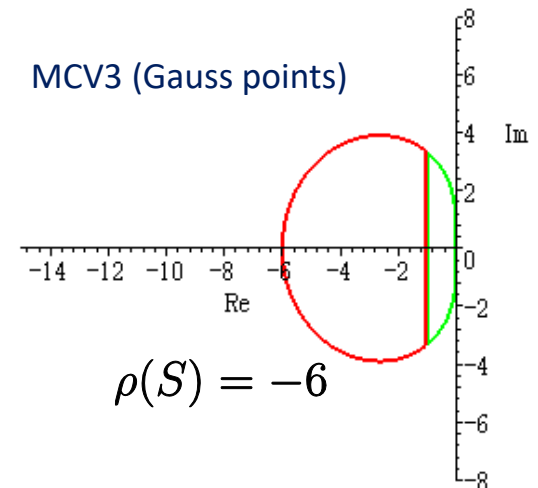
MCV3 (equi-spaced points)



$$\rho(S) = -6$$

Semidiscrete Spectra

MCV3 (Gauss points)



$$\rho(S) = -6$$

- Real part of the eigenvalues are negative (stable)
- The MCV3 schemes have smaller spectral radius and thus larger allowable CFL number for computational stability

Stable region of
3rd Runge-Kutta

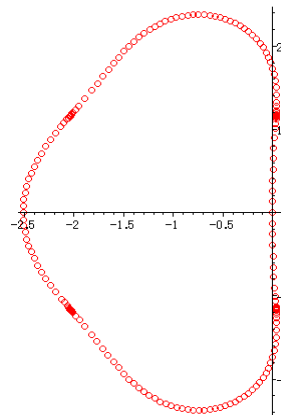


Table 3
 Normalized errors and convergence rates of the MCV type schemes.

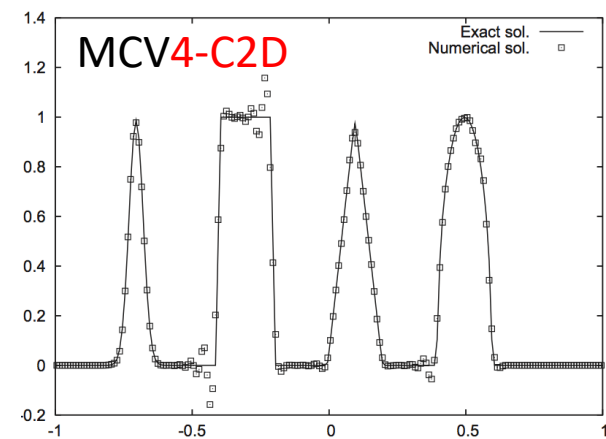
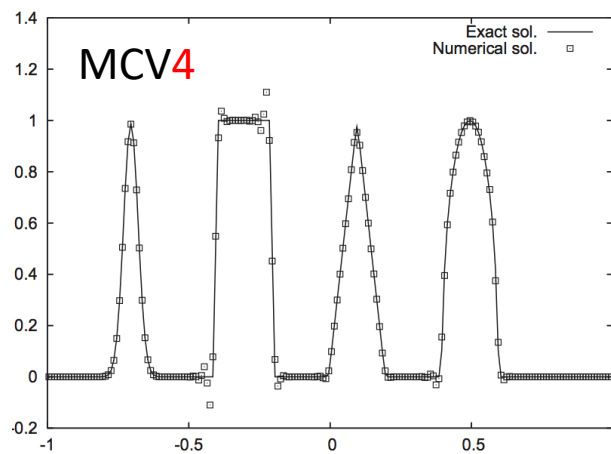
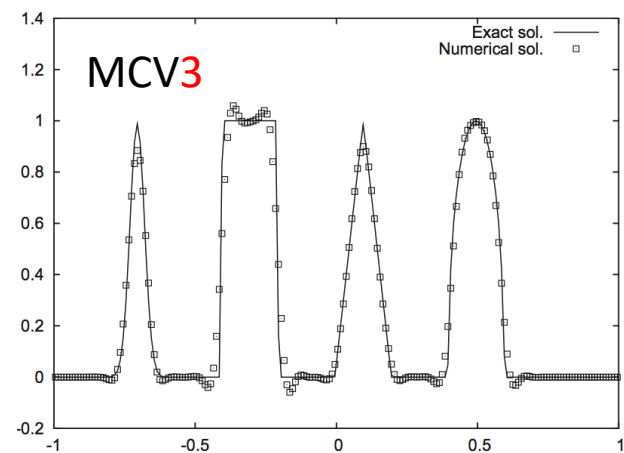
Convergence test

	Mesh	ℓ_1	ℓ_1 -Order	ℓ_2	ℓ_2 -Order	ℓ_∞	ℓ_∞ -Order
MCV3							
<u>3rd order</u>	10	1.29×10^{-2}	–	1.43×10^{-2}	–	2.03×10^{-2}	–
	20	1.69×10^{-3}	2.93	1.87×10^{-3}	2.93	2.69×10^{-3}	2.92
	40	2.14×10^{-4}	2.98	2.37×10^{-4}	2.98	3.37×10^{-4}	3.00
	80	2.68×10^{-5}	3.00	2.98×10^{-5}	2.99	4.22×10^{-5}	3.00
MCV4							
<u>4th order</u>	10	2.06×10^{-4}	–	2.26×10^{-4}	–	3.24×10^{-4}	–
	20	1.31×10^{-5}	3.98	1.46×10^{-5}	3.95	2.09×10^{-5}	3.95
	40	8.32×10^{-7}	3.98	9.25×10^{-7}	3.98	1.31×10^{-6}	4.00
	80	5.24×10^{-8}	3.99	5.82×10^{-8}	3.99	8.25×10^{-8}	3.99
MCV4_C2D							

Table 4
 Largest allowable CFL numbers.

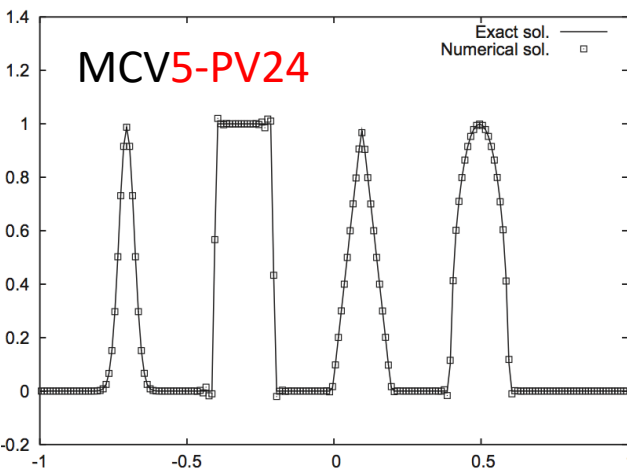
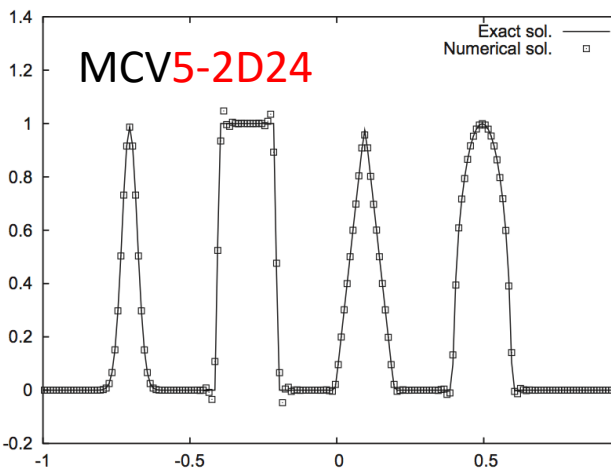
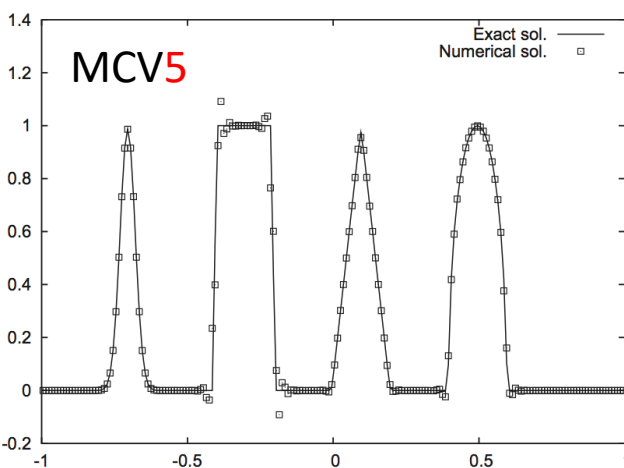
The allowable CFL number is larger than DG's

Schemes	MCV3	MCV4	MCV4_C2D	MCV5	MCV5_2D24	MCV5_PV24
CFL (max)	0.425	0.275	0.485	0.21	0.235	0.165
	10	5.21×10^{-5}	–	5.72×10^{-5}	–	8.18×10^{-5}
	20	1.67×10^{-6}	4.96	1.85×10^{-6}	4.95	2.65×10^{-6}
	40	5.28×10^{-8}	4.98	5.86×10^{-8}	4.98	8.31×10^{-8}
	80	1.65×10^{-9}	5.00	1.84×10^{-9}	4.99	2.61×10^{-9}
MCV5_2D24						
<u>5th order</u>	10	4.58×10^{-5}	–	5.02×10^{-5}	–	7.20×10^{-5}
	20	1.46×10^{-6}	4.97	1.62×10^{-6}	4.95	2.32×10^{-6}
	40	4.63×10^{-8}	4.99	5.13×10^{-8}	4.98	7.29×10^{-8}
	80	1.46×10^{-9}	4.99	1.62×10^{-9}	4.98	2.29×10^{-9}
MCV5_PV24						
	10	3.48×10^{-6}	–	3.85×10^{-6}	–	5.48×10^{-6}
	20	1.07×10^{-7}	5.02	1.18×10^{-7}	5.03	1.70×10^{-7}
	40	3.33×10^{-9}	5.01	3.70×10^{-9}	5.00	5.25×10^{-9}
	80	1.06×10^{-10}	4.97	1.17×10^{-10}	4.98	1.66×10^{-10}



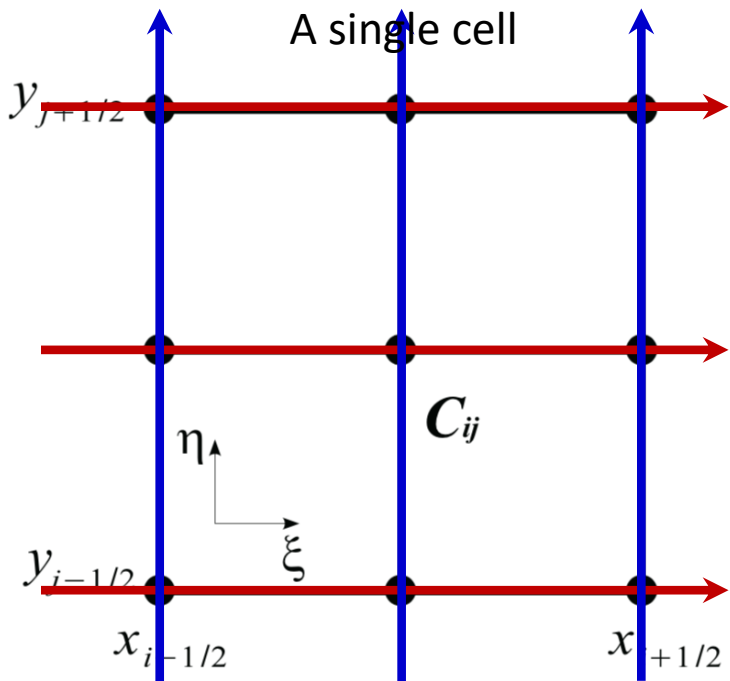
$$u(x,0) = \begin{cases} \frac{1}{6}(G(x, \beta, z - \delta) + G(x, \beta, z + \delta) + 4G(x, \beta, z)), & \text{for } -0.8 \leq x \leq -0.6, \\ 1, & \text{for } -0.4 \leq x \leq -0.2, \\ 1 - |10(x - 0.1)|, & \text{for } 0.0 \leq x \leq 0.2, \\ \frac{1}{6}(F(x, \alpha, a - \delta) + F(x, \alpha, a + \delta) + 4F(x, \alpha, a)), & \text{for } 0.4 \leq x \leq 0.6, \\ 0, & \text{otherwise,} \end{cases}$$

Jiang and Shu's test



Extension to multi-dimensions

For example, 3rd order MCV scheme



$$\mathcal{D} = \bigcup_{i,j=1}^{I,J} C_{ij}$$

$$C_{ij} = [x_{i-1/2}, x_{i+1/2}] \otimes [y_{j-1/2}, y_{j+1/2}]$$

$$\Delta x_i = x_{i+1/2} - x_{i-1/2} \quad \Delta y_j = y_{j+1/2} - y_{j-1/2}$$

$$\xi_1 = x_{i-\frac{1}{2}}, \quad \xi_2 = (x_{i-\frac{1}{2}} + x_{i+\frac{1}{2}})/2, \quad \xi_3 = x_{i+\frac{1}{2}};$$

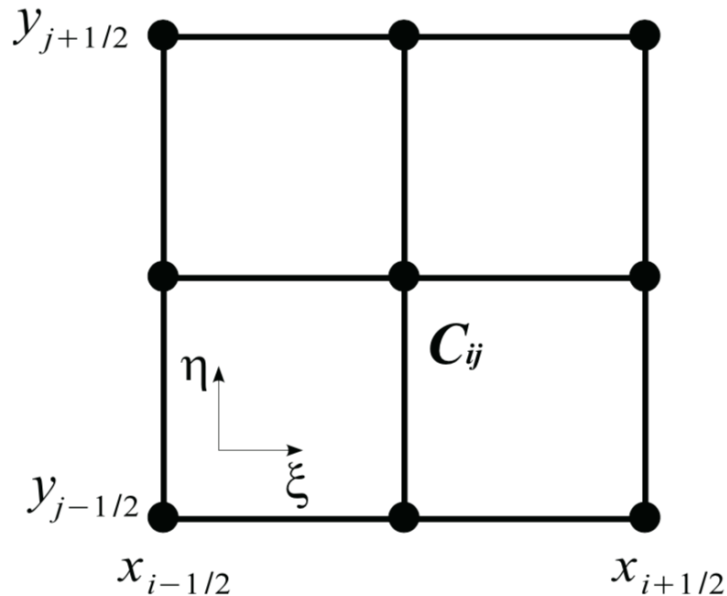
$$\eta_1 = y_{j-\frac{1}{2}}, \quad \eta_2 = (y_{j-\frac{1}{2}} + y_{j+\frac{1}{2}})/2, \quad \eta_3 = y_{j+\frac{1}{2}}$$

1D building block: the l th line segment $\overline{\xi_1 \xi_3} \times \eta_l, l = 1, 2, 3$

1D building block: the k th line segment $\xi_k \times \overline{\eta_1 \eta_3}, k = 1, 2, 3$

Extension to multi-dimensions

For example, 3rd order MCV scheme



$$\frac{\partial q}{\partial t} + \frac{\partial f}{\partial x} + \frac{\partial g}{\partial y} = 0$$

The semi-discretized equations for the point-value solutions within cell C_{ij}

$$\frac{d}{dt}(q_{kl}) = \sum_{\alpha=1}^4 \mathcal{M}_{k\alpha}^{(x)} \mathcal{F}_{\alpha} + \sum_{\beta=1}^4 \mathcal{M}_{l\beta}^{(y)} \mathcal{G}_{\beta},$$

$$\mathbf{M}^{(x)} = \begin{pmatrix} 0 & 0 & -1 & 0 \\ \frac{3}{2\Delta x_i} & -\frac{3}{2\Delta x_i} & \frac{1}{4} & \frac{1}{4} \\ 0 & 0 & 0 & -1 \end{pmatrix}$$

F: flux and its derivative at the end of ξ -line segment

$$\mathbf{F} = \left(\hat{f}_{i-\frac{1}{2}l}, \hat{f}_{i+\frac{1}{2}l}, \hat{f}_{xi-\frac{1}{2}l}, \hat{f}_{xi+\frac{1}{2}l} \right)^T$$

$$\mathbf{M}^{(y)} = \begin{pmatrix} 0 & 0 & -1 & 0 \\ \frac{3}{2\Delta y_j} & -\frac{3}{2\Delta y_j} & \frac{1}{4} & \frac{1}{4} \\ 0 & 0 & 0 & -1 \end{pmatrix}$$

G: flux and its derivative at the end of η -line segment

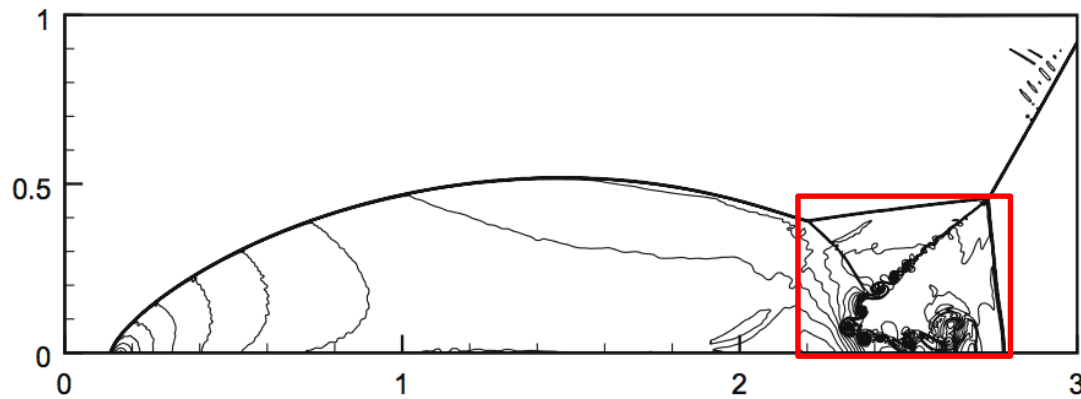
$$\mathbf{G} = \left(\hat{g}_{kj-\frac{1}{2}}, \hat{g}_{kj+\frac{1}{2}}, \hat{g}_{ykj-\frac{1}{2}}, \hat{g}_{ykj+\frac{1}{2}} \right)^T$$

double Mach reflection

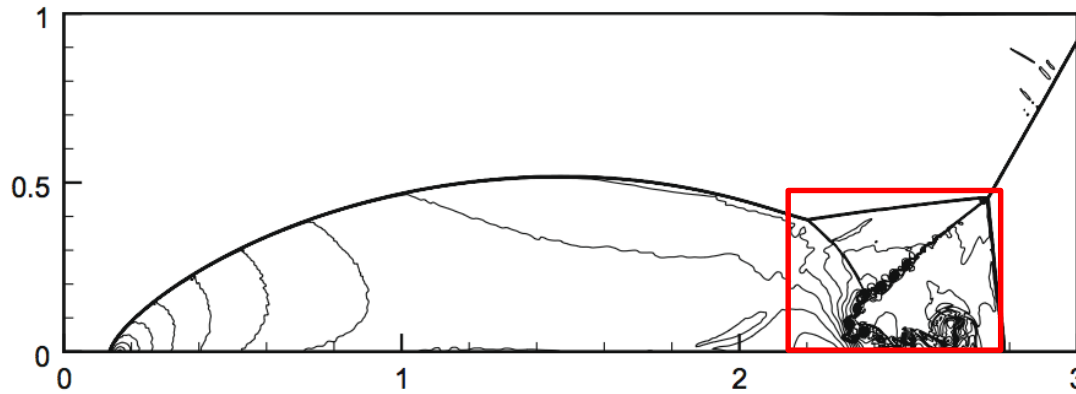
at $t = 0.2$

with 1440×480 cells

(li and Xiao, JCP, 2009)



(a) third-order



(b) fourth-order

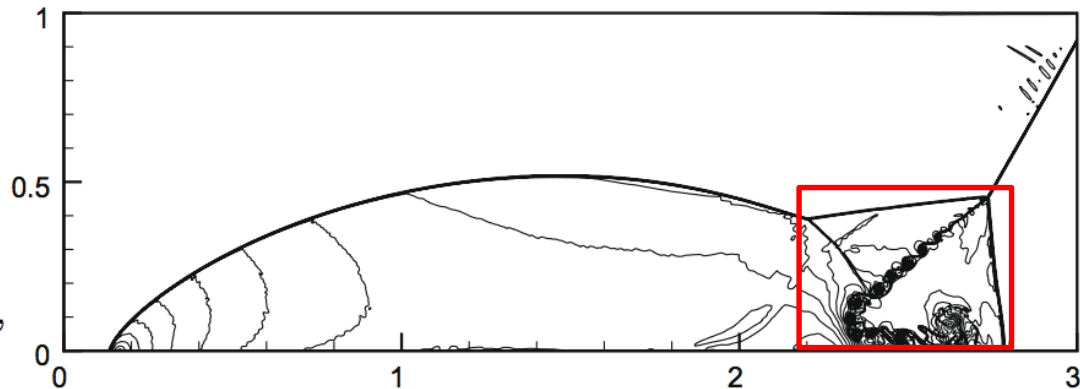
2D Euler equation

$$q_t + f(q)_x + g(q)_y = 0$$

$$q = (\rho, \rho u, \rho v, E)^T,$$

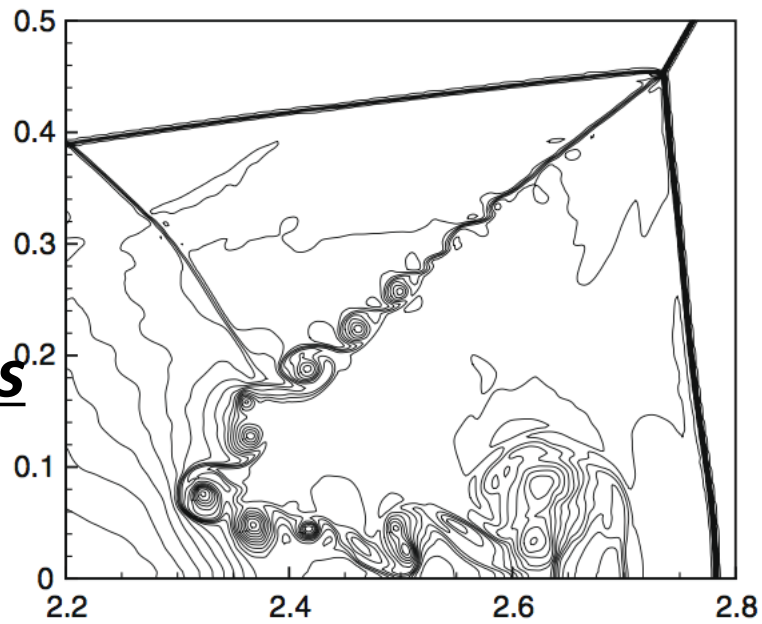
$$f(q) = (\rho u, \rho u^2 + p, \rho u v, u(E + p))^T,$$

$$g(q) = (\rho v, \rho u v, \rho v^2 + p, v(E + p))^T,$$

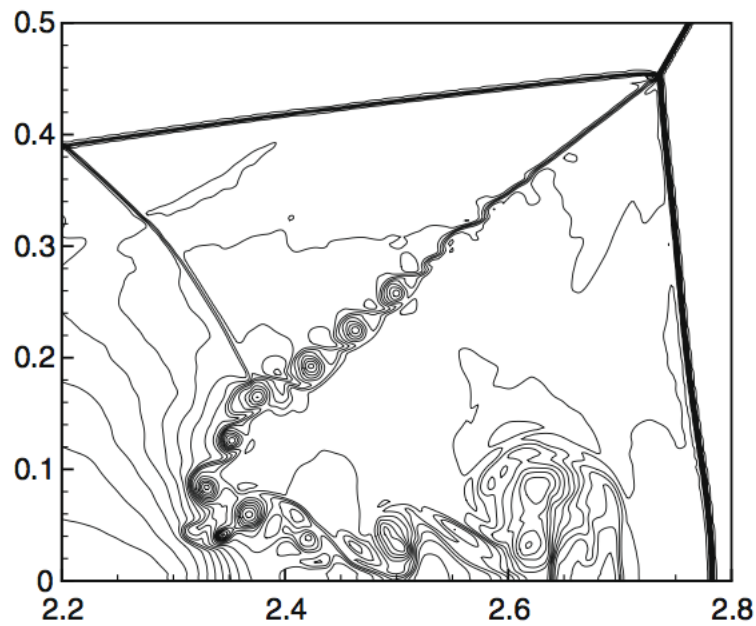


(c) fifth-order

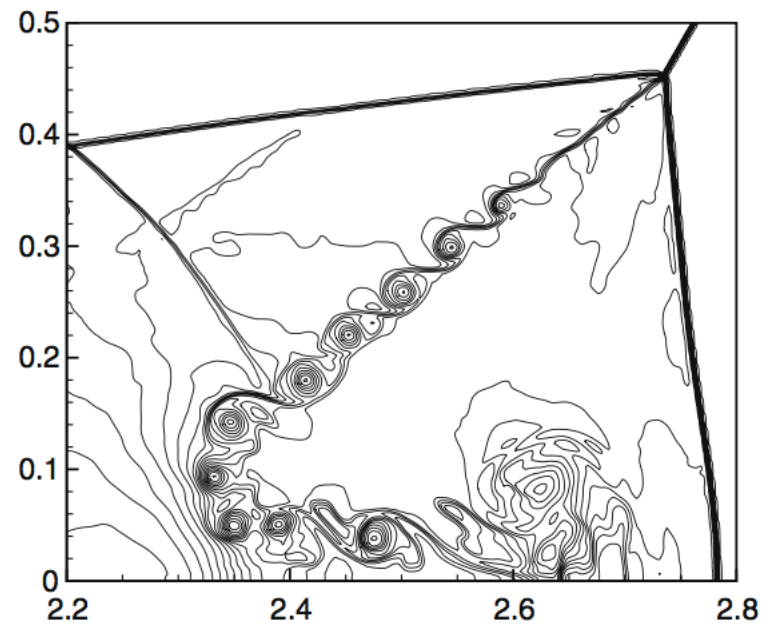
**The detailed shock
and vortex structures**



(a) third-order



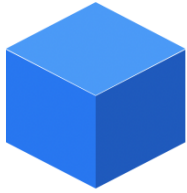
(b) fourth-order



(c) fifth-order

Some remarks of MMFV scheme

- ❑ The MCV schemes are high order, stable and nodal-form scheme.
- ❑ Exact numerical conservation
- ❑ The solution point location is not sensitive to the results, the equidistant solution point more attractive
- ❑ A Fourier analysis show the large allowable CFL number in comparison with the existing high order scheme like DG.
- ❑ No numerical quadrature is involved, so the source terms are easily handled



MM-FV DynCore on cubed sphere

- **Shallow water model and 2D nonhydrostatic model
-- benchmark results**

Shallow water model and 2D nonhydrostatic model

Shallow water equation

(Chen et al., 2014, JCP)

$$\frac{\partial(\sqrt{\Gamma}h)}{\partial t} + \left(\frac{\partial(\sqrt{\Gamma}h\tilde{u})}{\partial \xi} + \frac{\partial(\sqrt{\Gamma}h\tilde{v})}{\partial \eta} \right) = 0,$$

$$\frac{\partial u}{\partial t} + \frac{\partial(\Phi + K)}{\partial \xi} = -\sqrt{\Gamma}\tilde{v}(\mu + \zeta),$$

$$\frac{\partial v}{\partial t} + \frac{\partial(\Phi + K)}{\partial \eta} = -\sqrt{\Gamma}\tilde{u}(\mu + \zeta),$$

$$\Phi = g(h + h_s) \quad K = \frac{1}{2}\mathbf{v} \cdot \mathbf{v}$$

$$\zeta \equiv \mathbf{k} \cdot (\nabla \times \mathbf{v})$$

$\sqrt{\Gamma}$ is the Jacobian of the transformation

(u, v) and (\tilde{u}, \tilde{v})

the covariant and contravariant components

Nonhydrostatic equation

(Li et al., 2013, MWR)

$$\frac{\partial \mathbf{q}}{\partial t} + \frac{\partial \mathbf{f}}{\partial x} + \frac{\partial \mathbf{g}}{\partial \zeta} = \mathbf{s}(\mathbf{q})$$

$$\mathbf{q} = [\sqrt{G}\rho', \sqrt{G}\rho u, \sqrt{G}\rho w, \sqrt{G}(\rho\theta)']^T$$

$$\mathbf{f} = (\sqrt{G}\rho u, \sqrt{G}\rho u^2 + \sqrt{G}p', \sqrt{G}\rho w u, \sqrt{G}\rho\theta u)^T$$

$$\mathbf{g} = (\sqrt{G}\rho\tilde{w}, \sqrt{G}\rho u\tilde{w} + \sqrt{G}G^{13}p', \sqrt{G}\rho w\tilde{w} + p', \sqrt{G}\rho\theta\tilde{w})^T$$

$$\mathbf{s}(\mathbf{q}) = (0, 0, -\sqrt{G}\rho'g, 0)^T$$

$$\tilde{w} = \frac{d\zeta}{dt} = \frac{1}{\sqrt{G}}(w + \sqrt{G}G^{13}u)$$

$\sqrt{G} = \partial z / \partial \zeta$ Jacobian of the transformation

$G^{13} = \partial \zeta / \partial x$ is the contravariant metric

Some benchmark results

(Li et al., 2013, MWR; Chen et al., 2014, JCP)

■ *Shallow water on sphere*

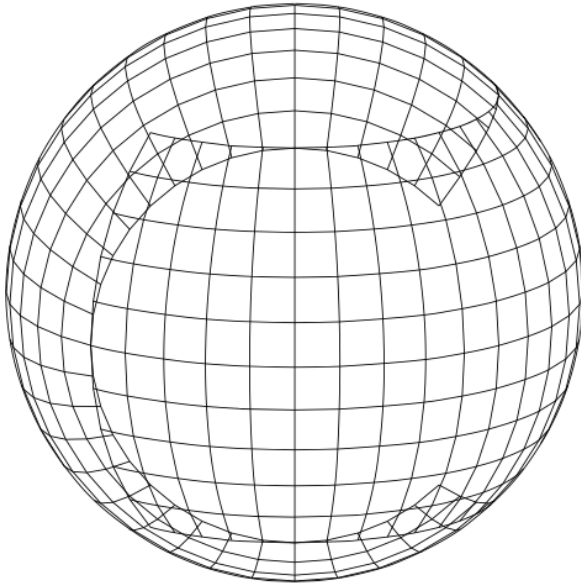
- ✓ *Advection*
- ✓ *Balance flow*
- ✓ *Mountain wave*
- ✓ *Rossby wave*
- ✓ *Barotropic instable flow*
- ✓ *Real test case*
- ✓ *...*

■ *Non-hydrostatic model*

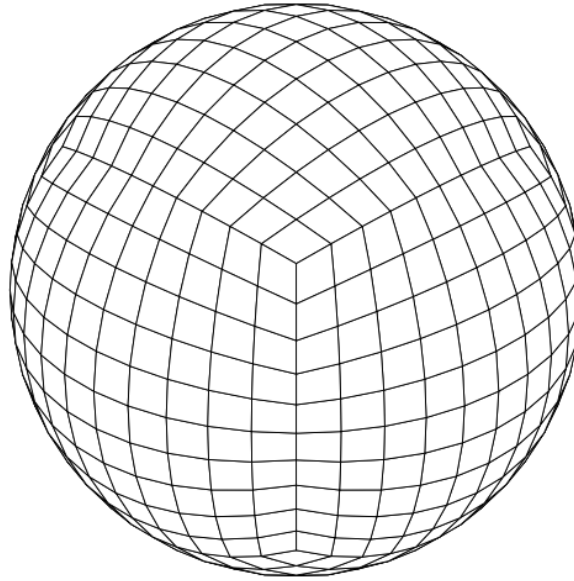
- ✓ *Rising thermal bubble*
- ✓ *Density current*
- ✓ *Internal gravity waves*
- ✓ *Hydrostatic mountain waves*
- ✓ *Non hydrostatic mountain waves*
- ✓ *Schär mountain waves*
- ✓ *...*

Selected SWE test cases

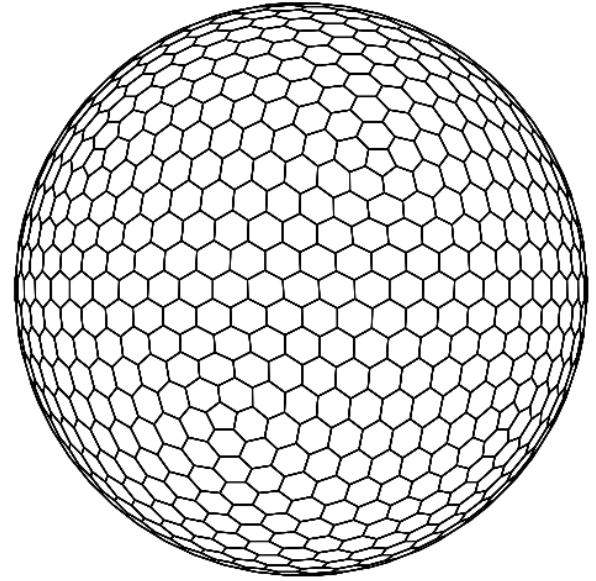
(Chen et al., 2014, JCP)



(a) Yin-Yang grid



(b) Cubed sphere grid



(c) Icosahedral-hexagonal grid

Table 1
The total numbers of the unknown DOFs in the third-order MCV models for different spherical grids.

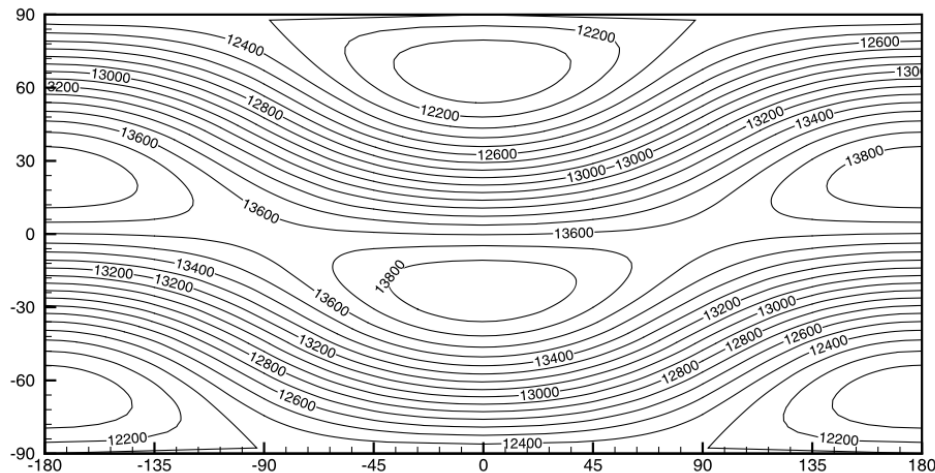
Spherical grid	Yin-Yang	Cubed-sphere	Icosahedral-hexagonal
Total DOFs	$24N^2 + 16N + 2$	$24N^2 + 2$	$30N^2 + 2$

Table 2
Minimum and maximum area ratio of different grids.

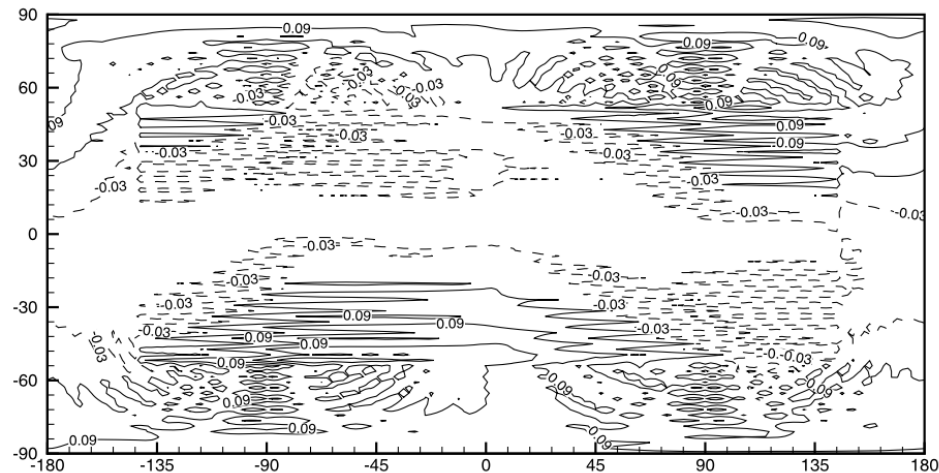
Yin-Yang grid	Cubed-sphere grid	Icosahedral grid with pentagonal cells	Icosahedral grid without pentagonal cells
0.7628 ($N = 10$)	0.7666 ($N = 10$)	0.6263 ($N = 9$)	0.8654 ($N = 9$)
0.7349 ($N = 20$)	0.7359 ($N = 20$)	0.6216 ($N = 18$)	0.8558 ($N = 18$)
0.7210 ($N = 40$)	0.7213 ($N = 40$)	0.6197 ($N = 36$)	0.8524 ($N = 36$)
0.7140 ($N = 80$)	0.7142 ($N = 80$)	0.6191 ($N = 72$)	0.8513 ($N = 72$)

SWE test case: Time dependent balanced zonal flow

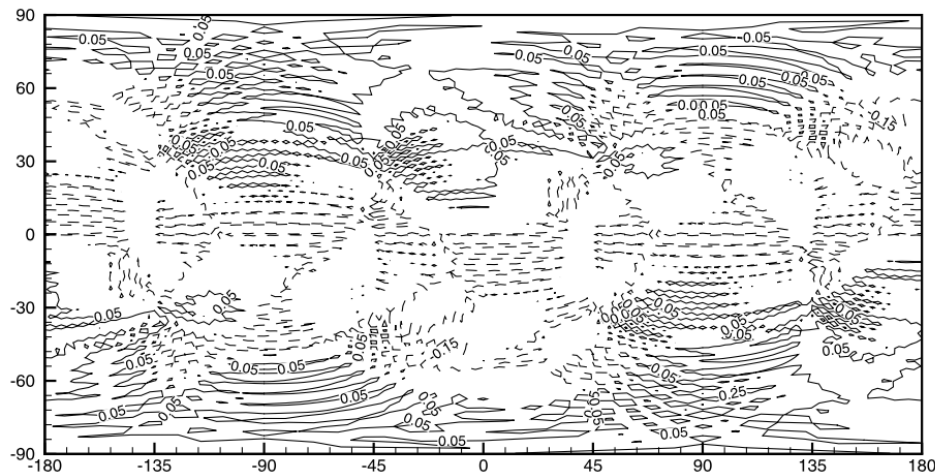
(Läuter et al., JCP, 2005)



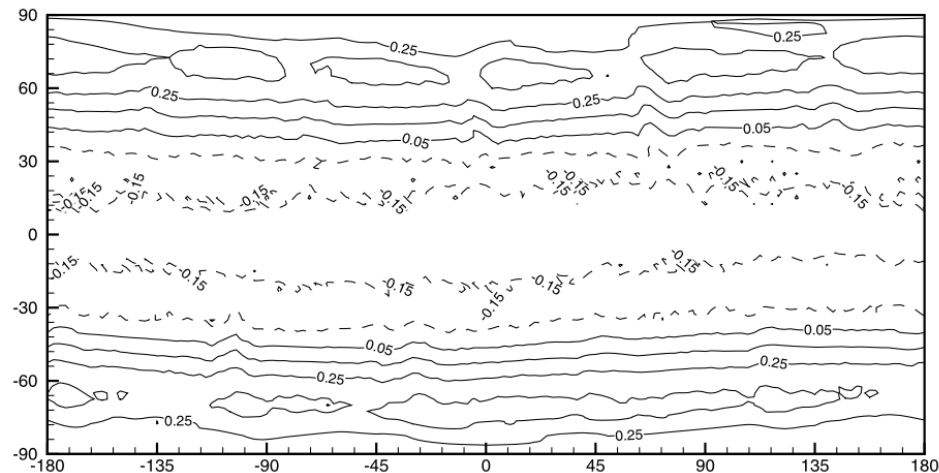
(a) The height field on cubed-sphere grid ($N = 20$).



(b) The absolute error on Yin-Yang grid ($N = 20$).



(c) The absolute error on cubed-sphere grid ($N = 20$).

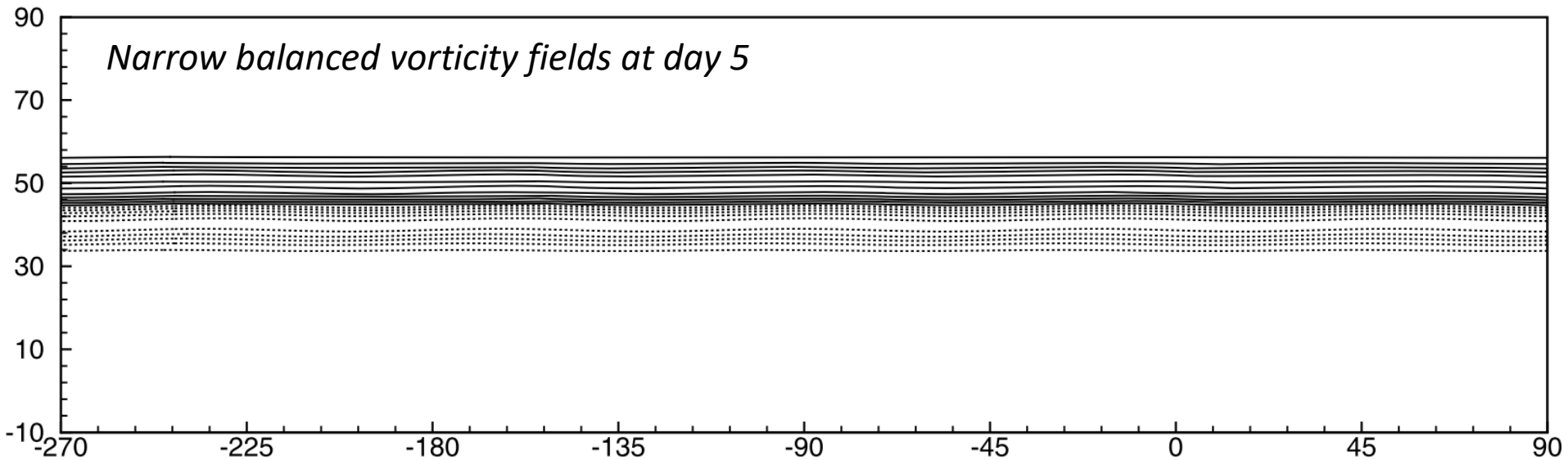


(d) The absolute error on icosahedral grid ($N = 18$).

Absolute errors \rightarrow grid imprinting

SWE test case: Barotropic jet flow

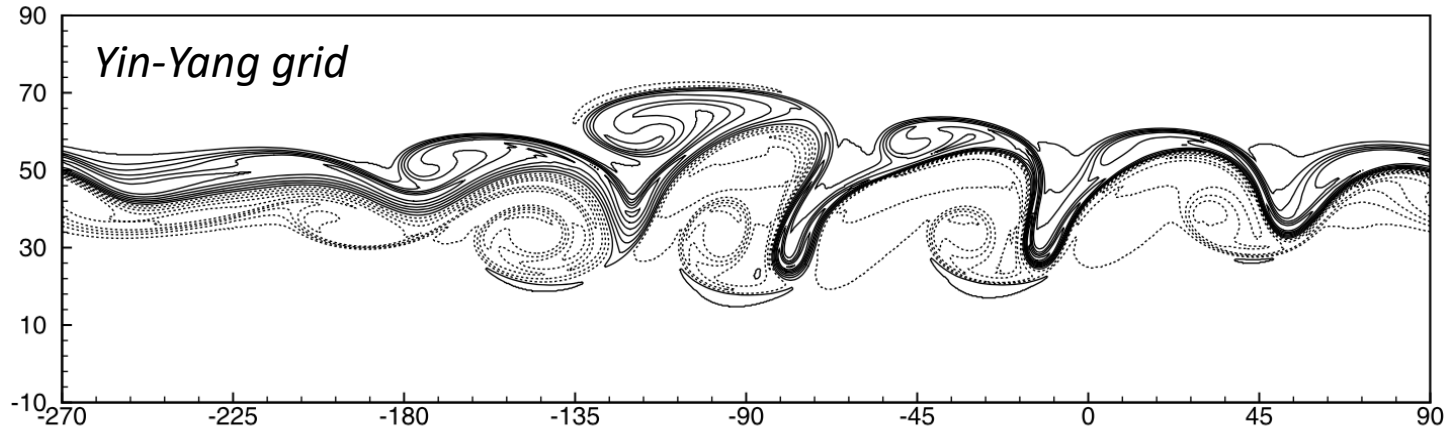
(Galewsky et al., Tellus, 2004)



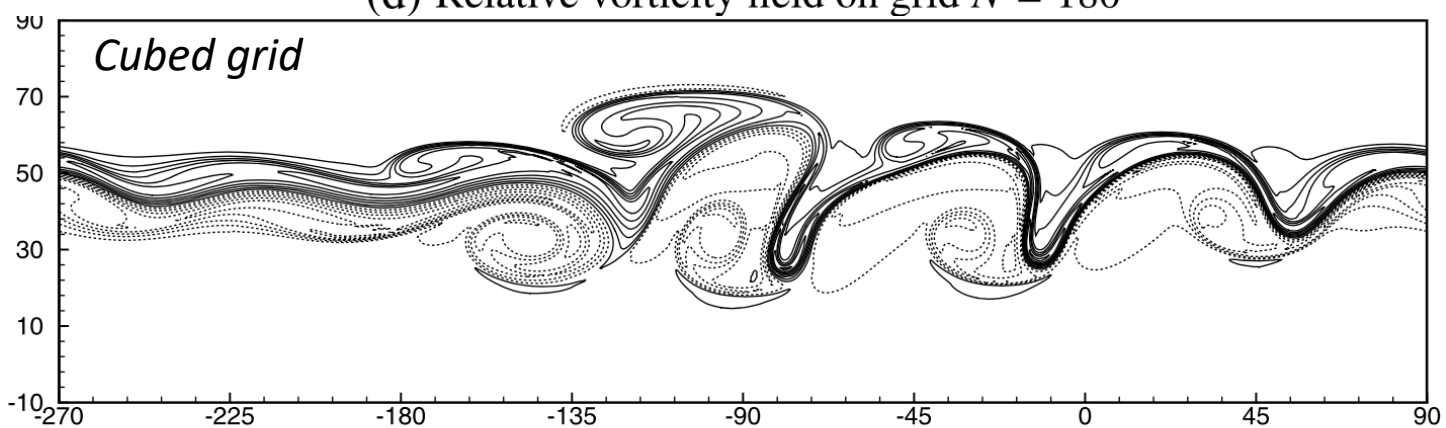
$$\text{Zonal velocity component } u(\phi) = \begin{cases} 0 & \text{for } \phi \leq \phi_0 \\ \frac{u_{\max}}{e_n} \exp \left[\frac{1}{(\phi - \phi_0)(\phi - \phi_1)} \right] & \text{for } \phi_0 < \phi < \phi_1 \\ 0 & \text{for } \theta \geq \phi_1 \end{cases}$$

The triggering perturbation height $h'(\lambda, \phi) = \hat{h} \cos(\phi) e^{-(\lambda/\alpha)^2} e^{-[(\phi_2 - \phi)/\beta]^2}$

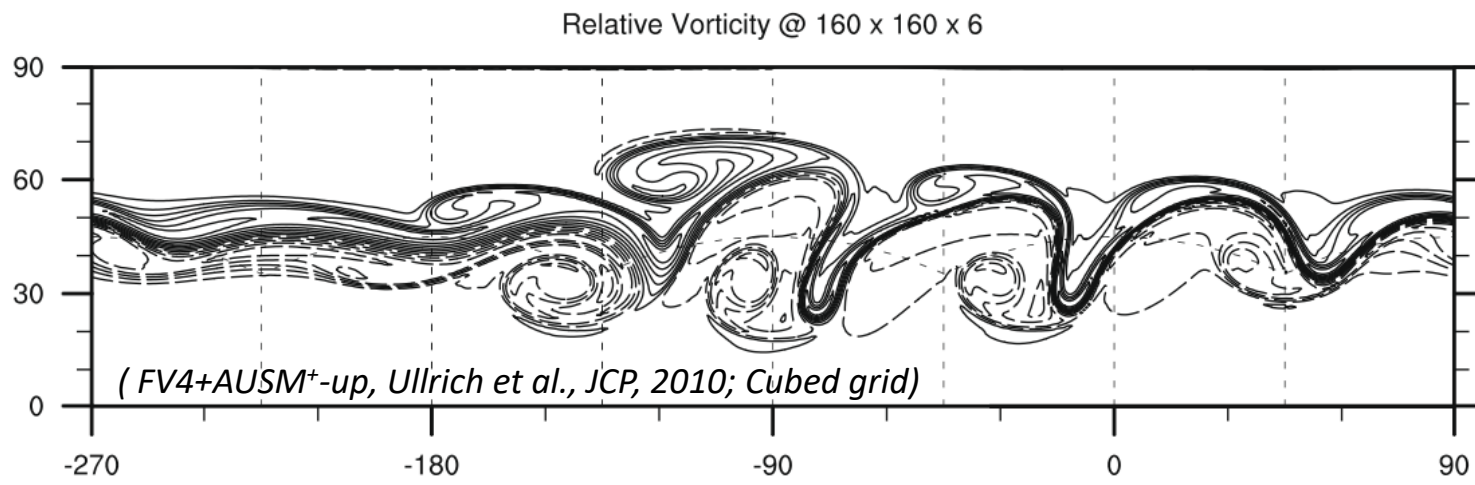
for $-\pi < \lambda < \pi,$



(d) Relative vorticity field on grid $N = 180$

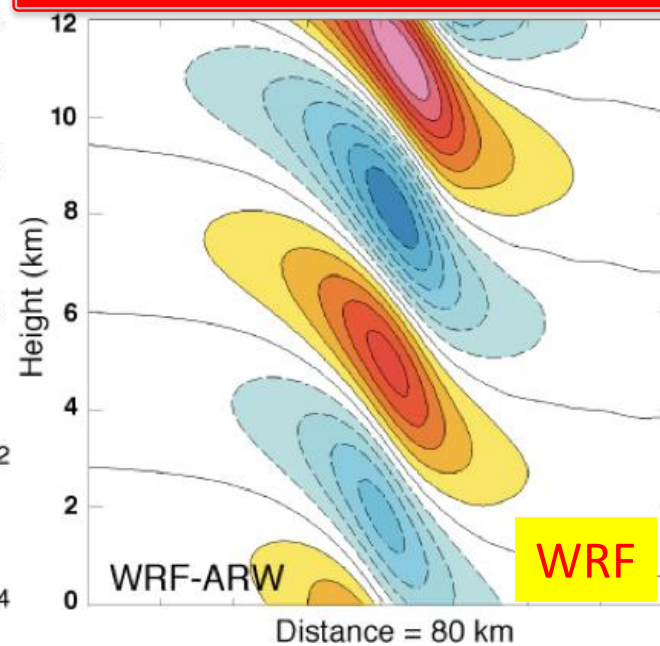
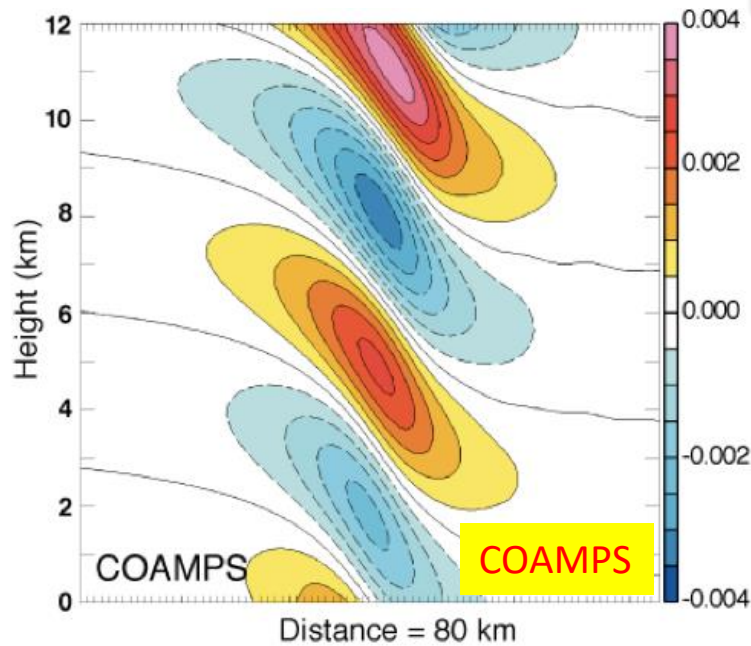
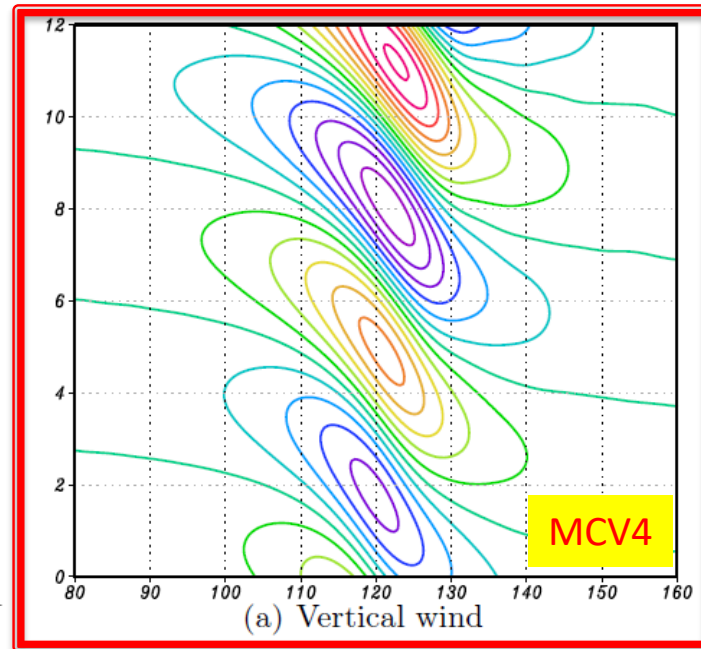
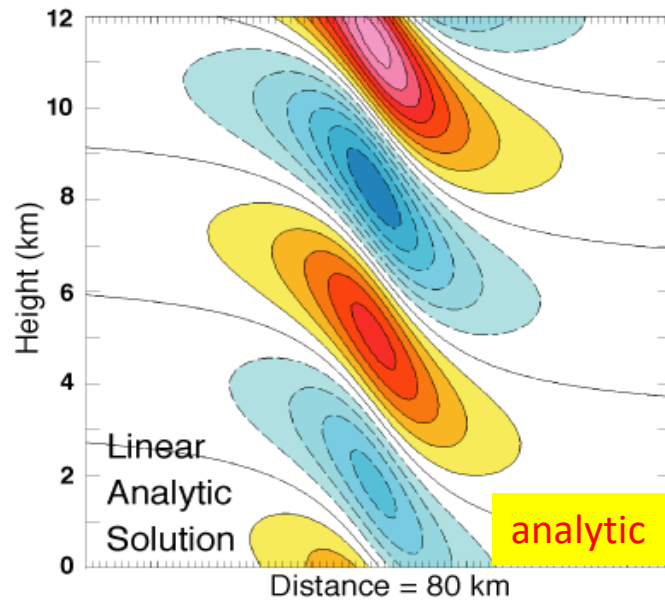


(d) Relative vorticity field on grid $N = 180$

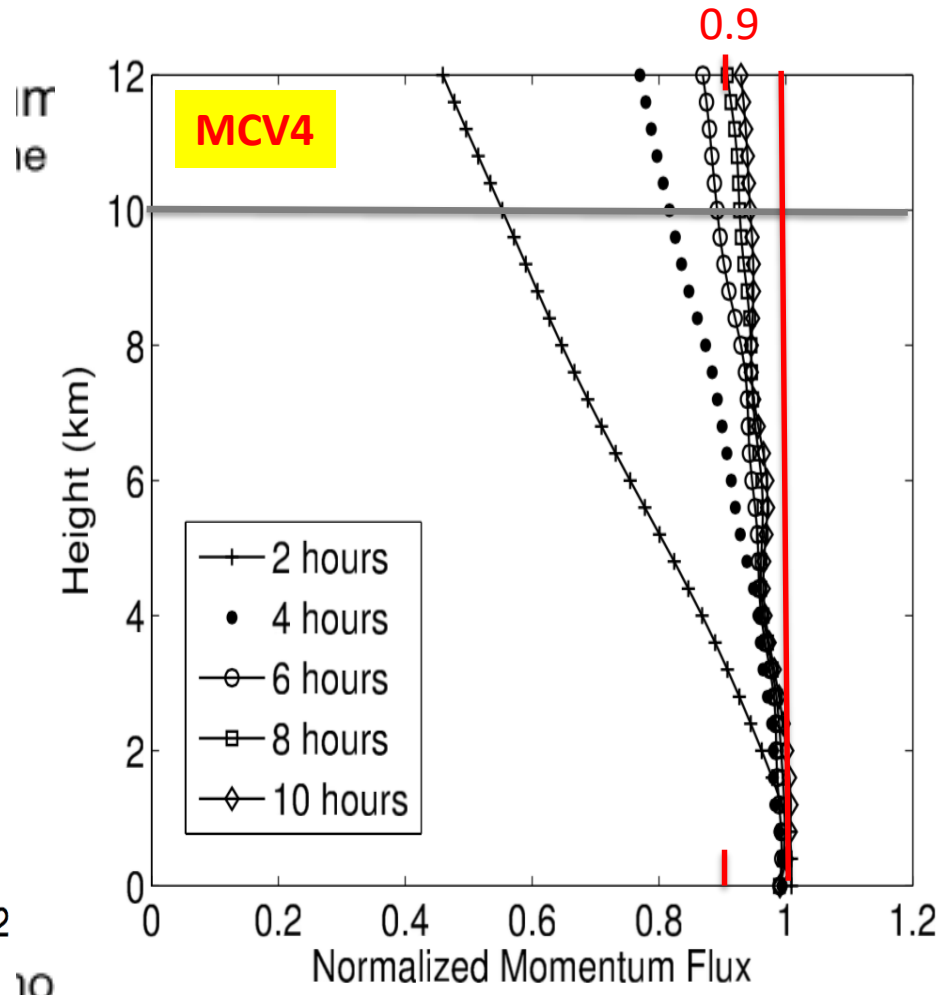
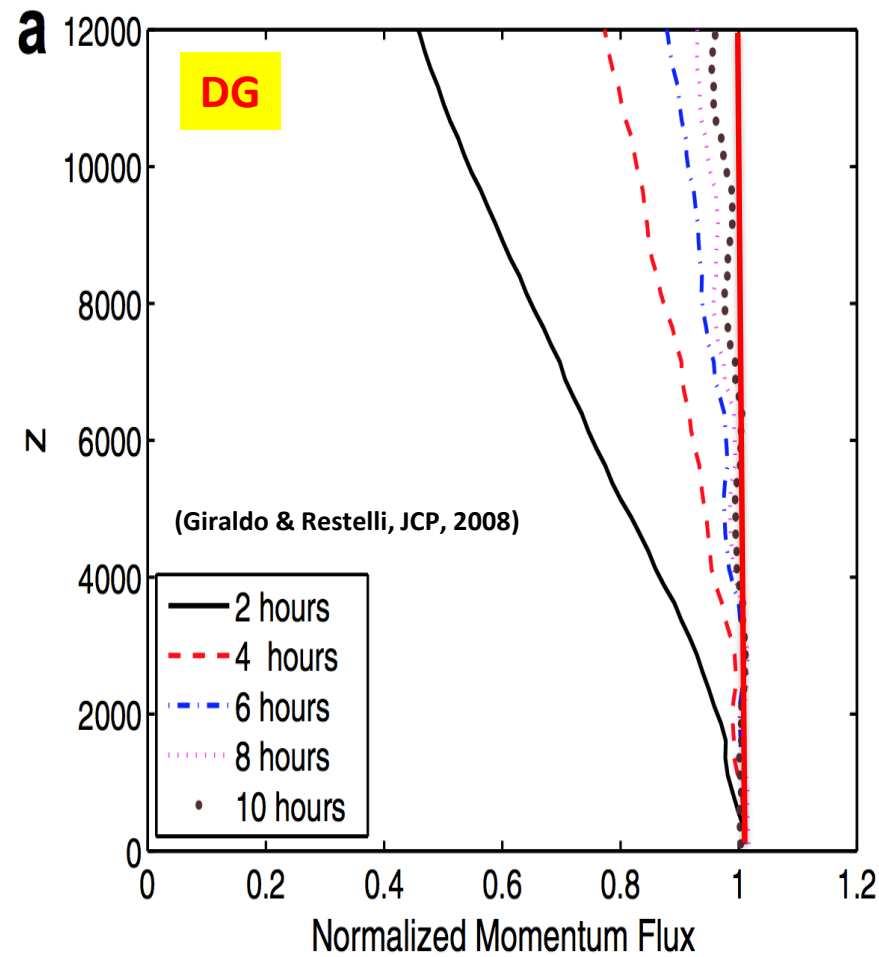


Benchmark: hydrostatic mountain waves

(Li et al., AIM, 2016)



Comparison with FV model for hydrostatic mountain waves

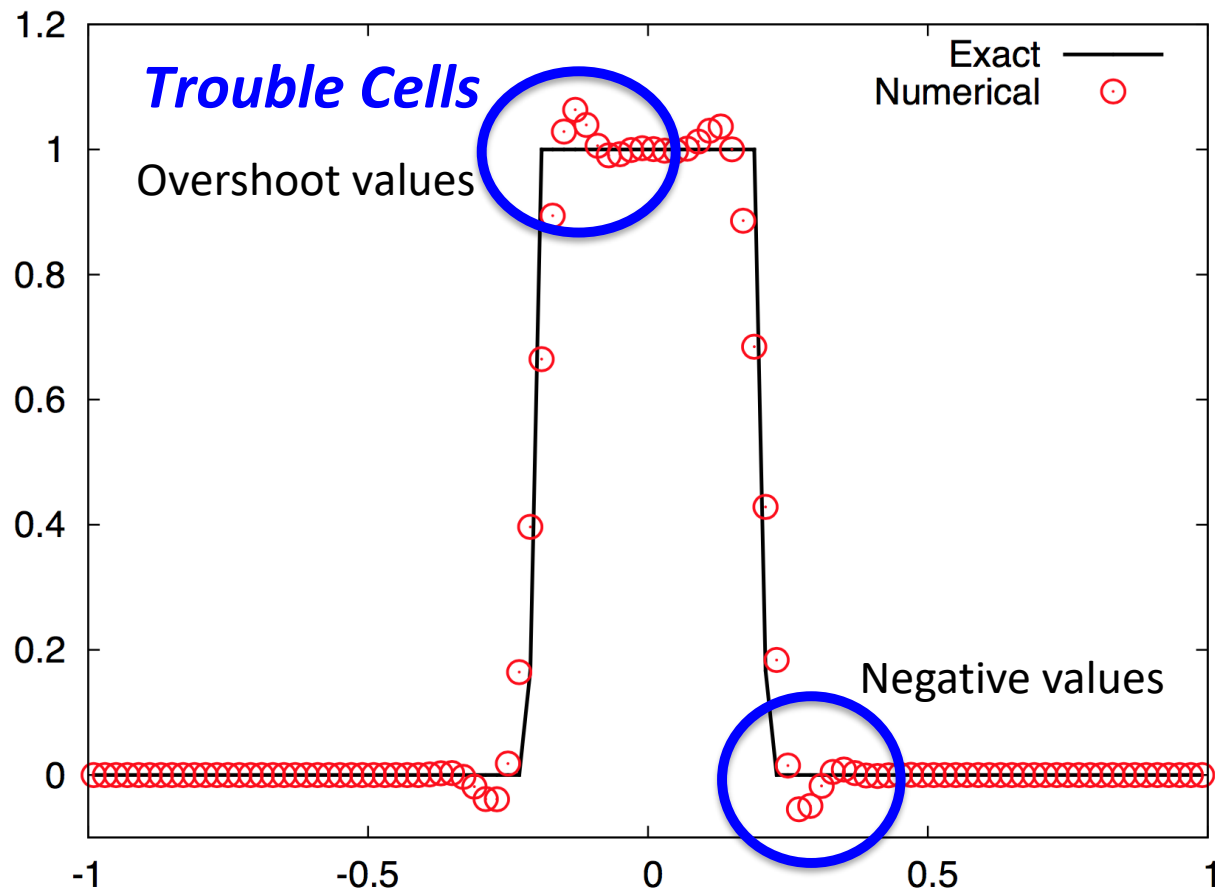


■ The limiting projection of MMFV scheme

High order scheme (≥ 2) always generate the numerical oscillations

Notable upwind schemes with limiter such as FCT, MUSCL, MPDATA, ENO, TVD, PPM, TVB, WENO can achieve the non-oscillatory properties for sharp gradients such as cold fronts, dryline, cloud boundaries and inversions.

High order schemes such as SE, DG need them.



High-order transport model in the MM-FV DynCore

$$\frac{\partial(\rho\phi_k)}{\partial t} + \nabla \cdot (\rho\phi_k \mathbf{v}) = 0 \quad \phi_k \text{ are transport fields}$$

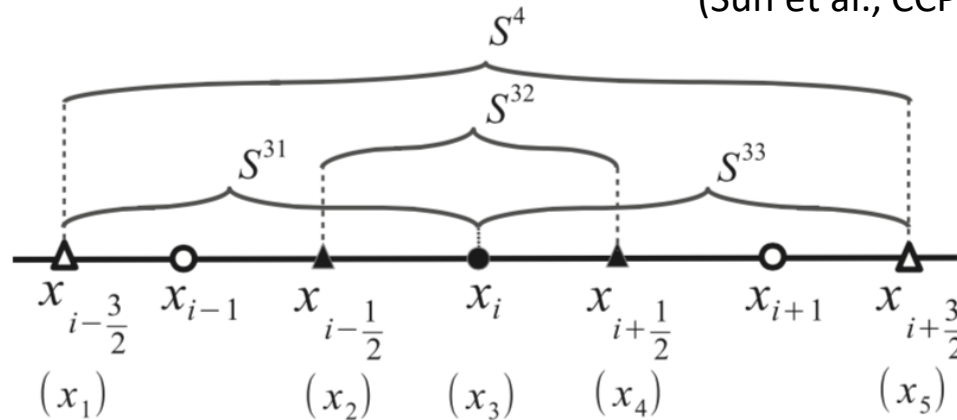
Options:

- Vertical
- Conservative Semi-Lagrangian with Rational function (**CSLR**)
(Xiao et al., JGR, 2002)
 - Piecewise rational method (**PRM**)
(Xiao and Peng, JCP, 2004)

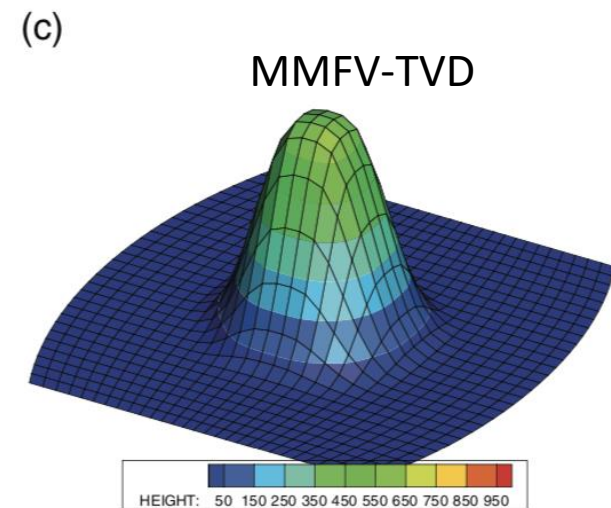
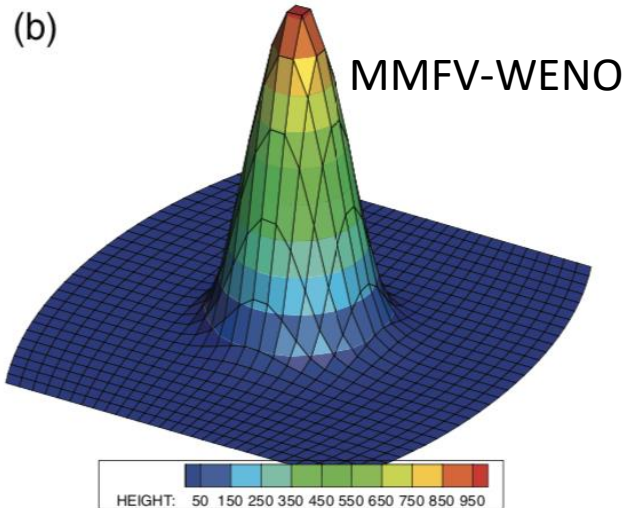
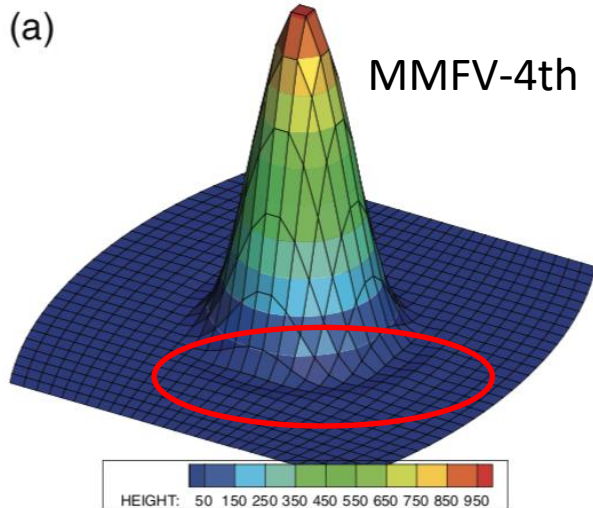
- Horizontal
- MCV 3-point scheme with 4th order **WENO**
(Sun et al., CCP, 2015, Tang et al., QJRMS, 2018)
 - MCV 3-point scheme with 4th order **BGS**
(Deng et al., JSC, 2017)
 - MCV 3-point scheme with **FCT** techniques
(Li et al., QJRMS, 2020)

Non-oscillatory MMFV-WENO limiter

(Sun et al., CCP, 2015, Tang et al., QJRM, 2018)



Stencils for determining slope parameter using the WENO concept for cell



Based on WENO concept, a slope limiter for a non-oscillatory scheme has the form

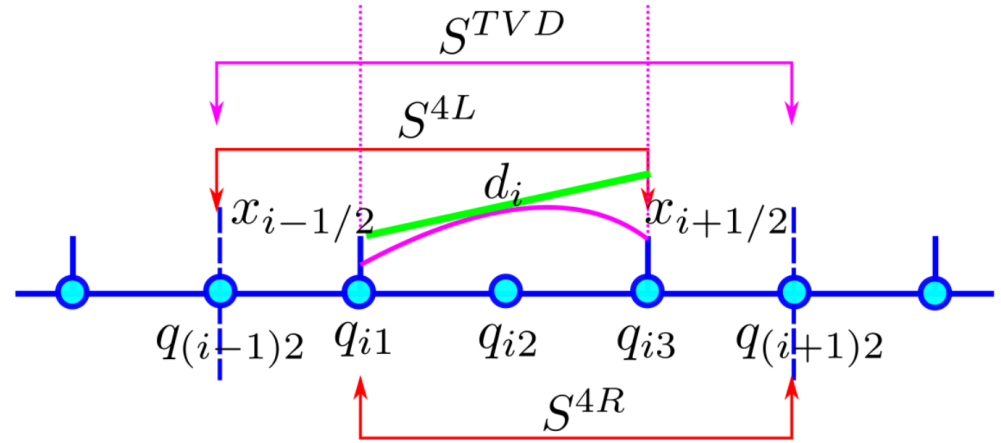
$$d_i^{\text{WENO}} = \omega_1 d_i^{31} + \omega_2 d_i^{32} + \omega_3 d_i^{33}$$

High order non-oscillatory BGS limiter

(Deng et al., J. Sci. Comput., 2017)

Boundary Gradient Switching (BGS)

(Basic idea similar to ENO)



$$\text{BGS} \left[\left(\frac{\partial Q_i(x)}{\partial x} \right)_{i-\frac{1}{2}} \right] =$$

$$\begin{cases} \text{dmin}(\mathbf{d}_1, \mathbf{d}_2) & \text{if } \text{sign}(\mathbf{d}_1) = \text{sign}(\mathbf{d}_2) = \text{sign}(\mathbf{d}_3) \\ \mathbf{d}_1 & \text{only if } \text{sign}(\mathbf{d}_1) = \text{sign}(\mathbf{d}_3) \\ \mathbf{d}_2 & \text{only if } \text{sign}(\mathbf{d}_2) = \text{sign}(\mathbf{d}_3) \\ \text{absmin}(\mathbf{d}_1, \mathbf{d}_2) & \text{otherwise} \end{cases}$$

$$\mathbf{d}_1 = \left(\frac{\partial Q_i^{4L}(x)}{\partial x} \right)_{i-\frac{1}{2}}$$

$$\mathbf{d}_2 = \left(\frac{\partial Q_i^{4R}(x)}{\partial x} \right)_{i-\frac{1}{2}}$$

$$\mathbf{d}_3 = \left(\frac{\partial Q_i^{TVD}(x)}{\partial x} \right)_{i-\frac{1}{2}}$$

$$\text{dmin}(\mathbf{d}_1, \mathbf{d}_2) = \begin{cases} \mathbf{d}_1 & \text{if } |\mathbf{d}_1 - \mathbf{d}_3| < |\mathbf{d}_2 - \mathbf{d}_3| \\ \mathbf{d}_2 & \text{otherwise} \end{cases}$$

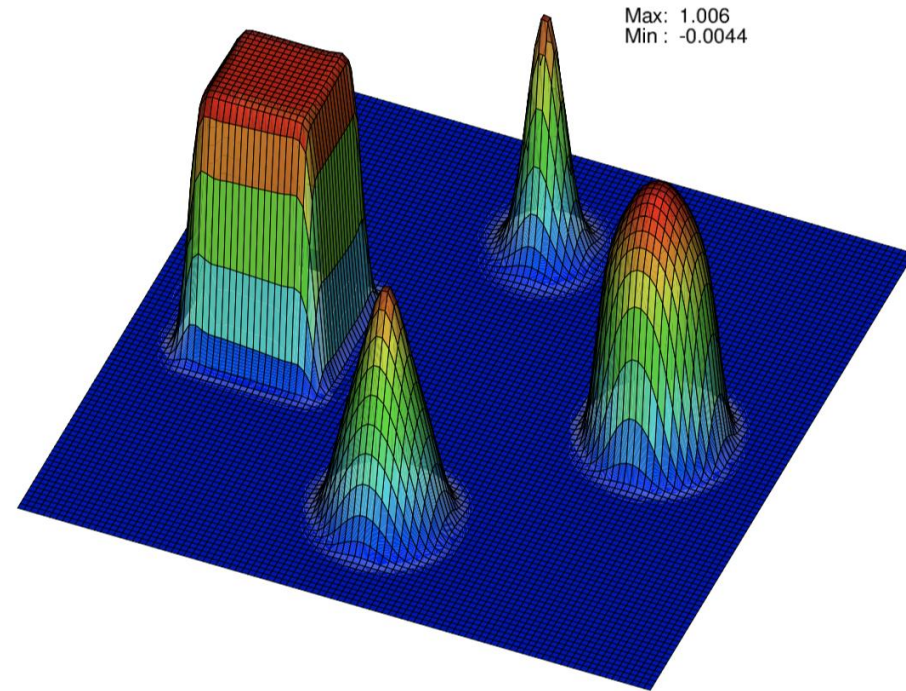
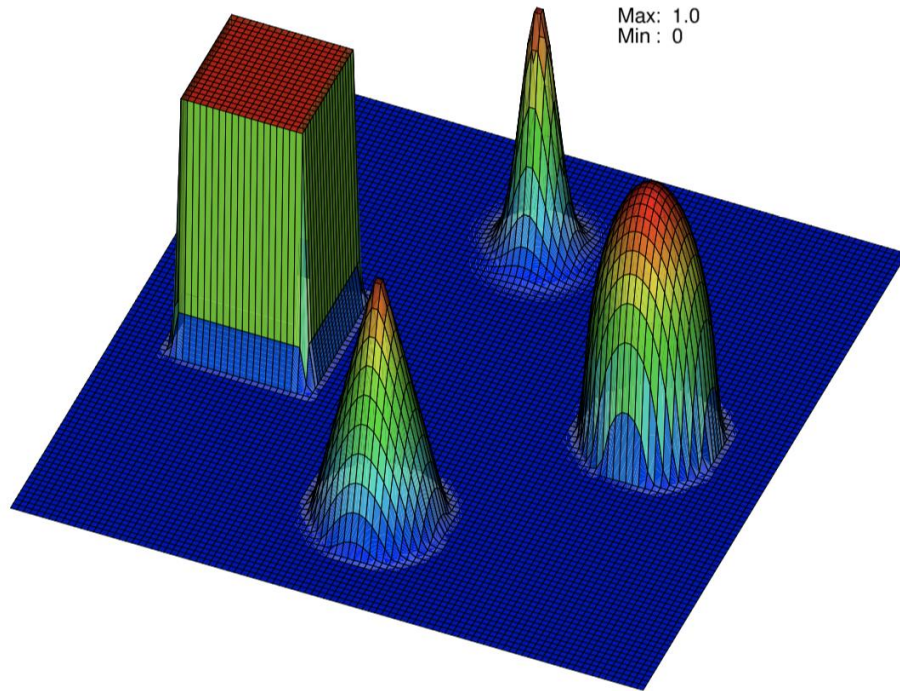
$$\text{absmin}(\mathbf{d}_1, \mathbf{d}_2) = \begin{cases} \mathbf{d}_1 & \text{if } |\mathbf{d}_1| < |\mathbf{d}_2| \\ \mathbf{d}_2 & \text{otherwise} \end{cases}$$

High order slope constrained BGS limiter

(Deng et al., J. Sci. Comput., 2017)

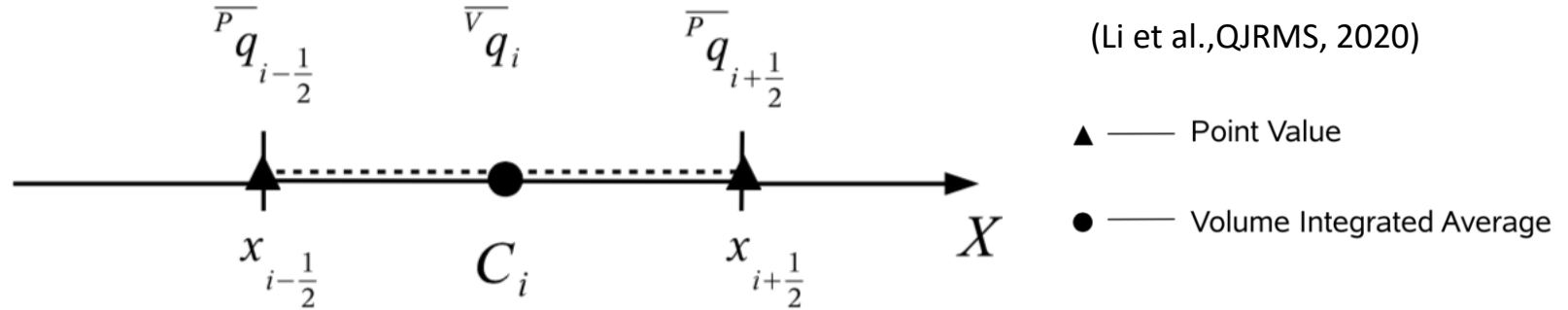
Convergence test (3 point MCV with Boundary Gradient Switching (BGS) limiter)

Grid number	40		80		160		320	
Errors/orders	1.66e-5	-	1.12e-6	3.80	7.87e-6	3.93	4.96e-9	3.99



- ✧ The compact local MCV3-BGS make full use of local information.
- ✧ No trouble cell indicators
- ✧ Do not suffer from loss of accuracy.

Non-negativity correction for MMFV transport model



$$\frac{\partial \overline{V}q_i}{\partial t} = \delta \mathcal{M}_i = -\frac{1}{\Delta x} \left(f_{i+\frac{1}{2}} - f_{i-\frac{1}{2}} \right)$$

Runge-Kutta substage:

$$\begin{cases} \overline{V}q_i^{(0)} &= \overline{V}q_i^n \\ \overline{V}q_i^{(s)} &= \overline{V}q_i^n + \Delta t \sum_{p=0}^{s-1} a_{sp} \delta \mathcal{M}_i^{(p)} \quad (s = 1 \text{ to } S) \\ \overline{V}q_i^{n+1} &= \overline{V}q_i^{(S)} \end{cases}$$

Constrained condition:

$$\frac{\overline{V}q_i^n}{\Delta t} + \sum_{p=0}^3 a_{4p} \delta \mathcal{M}_i^{(p)} \geq 0$$

A modified PV as followed

$$\left(\overline{P}q_{i-\frac{1}{2}}^{(s)} \right)^{\text{mod}} = \begin{cases} \theta_{i-1} \overline{P}q_{i-\frac{1}{2}}^{(s)} & \text{if } f_{i-\frac{1}{2}} \geq 0 \\ \theta_i \overline{P}q_{i-\frac{1}{2}}^{(s)} & \text{if } f_{i-\frac{1}{2}} < 0 \end{cases}$$

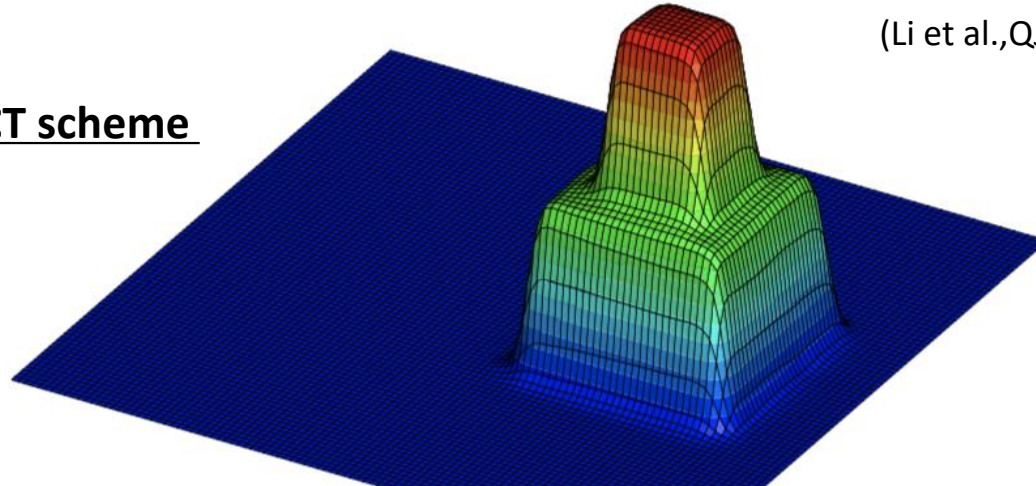
$$\theta_i = \min \left(1, \frac{\mathcal{M}_i}{\mathcal{M}_{\text{out}_i}^{(s)} + \epsilon} \right)$$

(Durrant 2010, Springer)

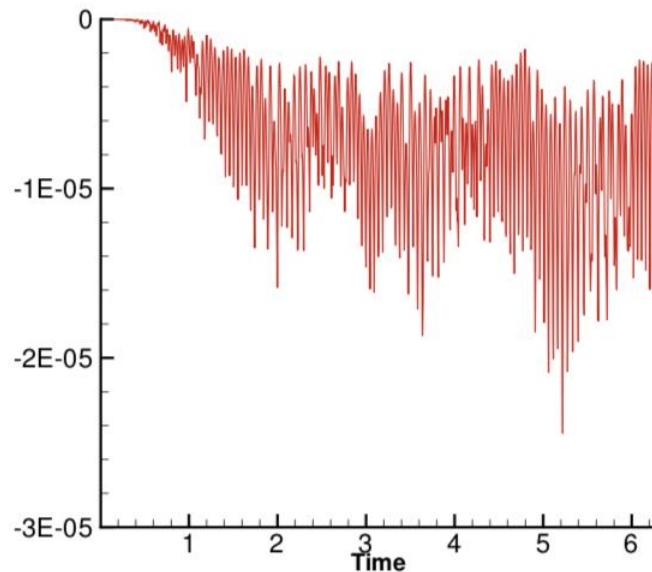
Example: Solid rotation of square cylinder

(Li et al., QJRMS, 2020)

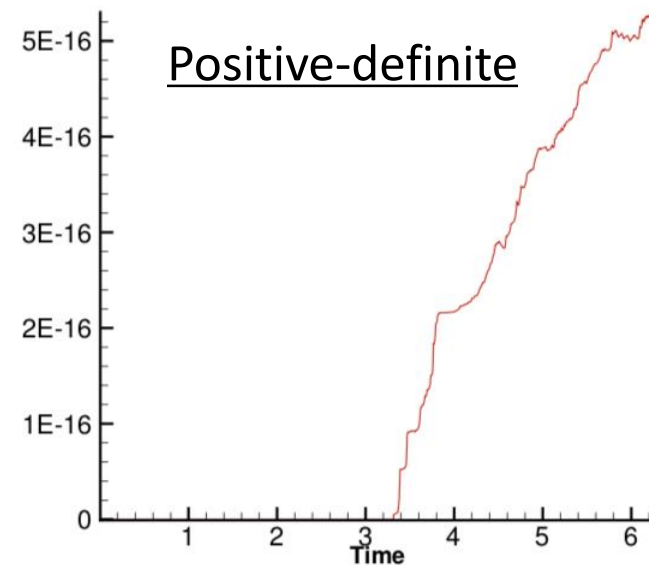
MMFV WENO FCT scheme



$t = 2\pi$ on grid 100×100

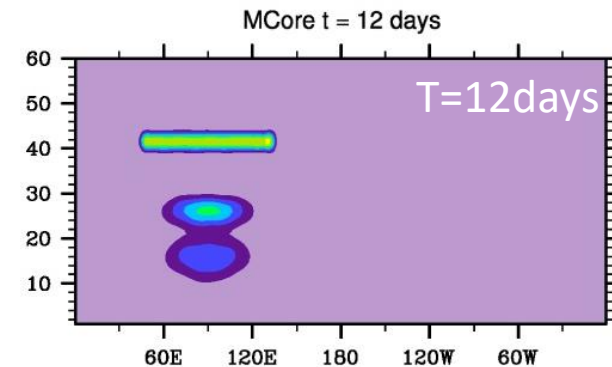
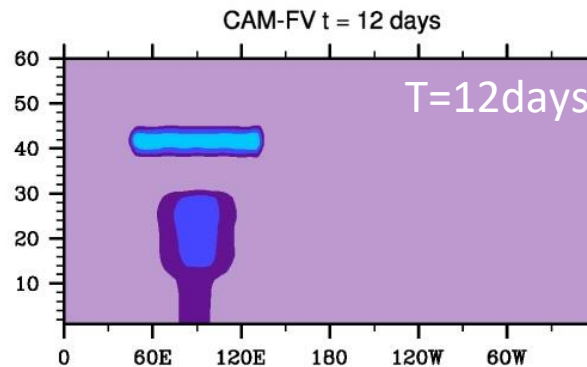
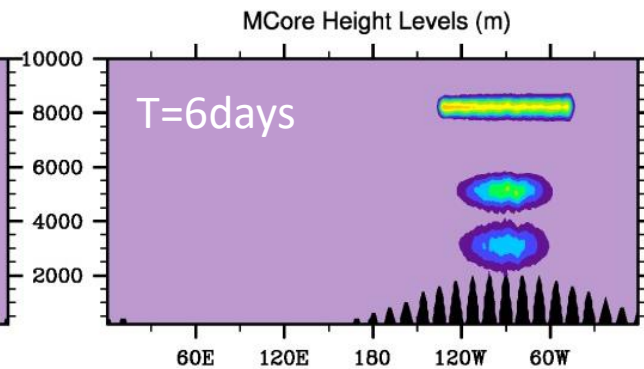
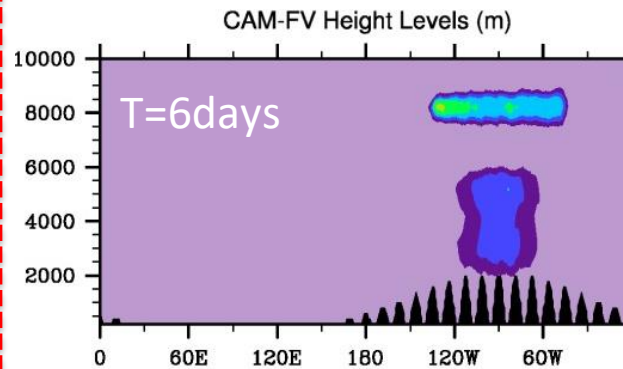
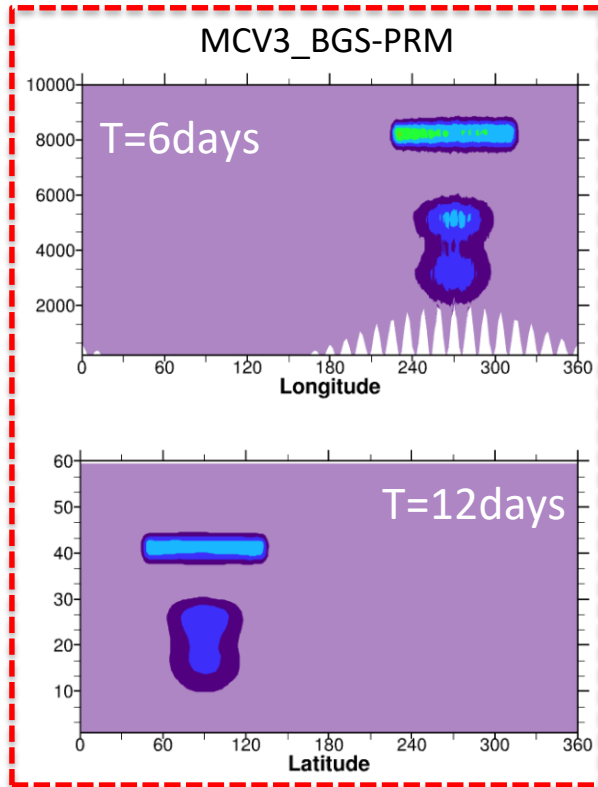


(a) maximum (a) and minimum (b) errors



(b)

3D advection of three thin cloud-like tracers over complex orography



Height-based terrain
following coordinate

(Gal-Chen and Somerville, 1975)

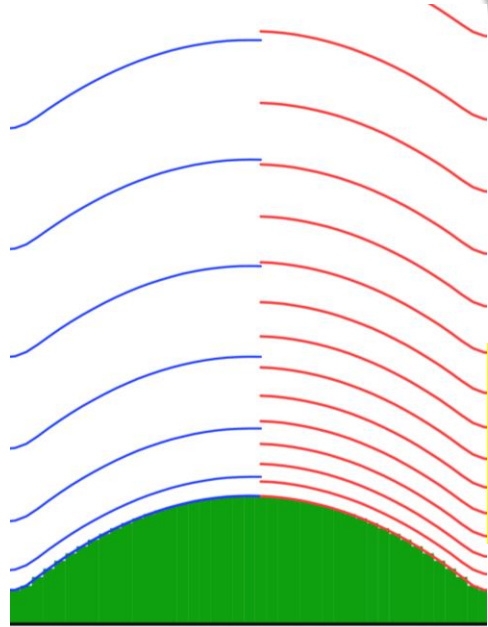


$$\Delta_{DOF} \approx 1^\circ, 121 \text{ levels}, 12 \text{ km}$$

(Kent et al., QJRM, 2014)

■ MMFV time marching

Need computational efficiency in atmospheric model

$$\frac{\partial \mathbf{q}}{\partial t} + \dots = \underbrace{Q_p}_{\text{pressure gradient}} + \underbrace{Q_S}_{\text{Source: fast physics et al.}}$$


- Sound/gravity wave
- stiff terms
- Vertical grid spacing is very small in PBL

A robust and efficient time marching scheme:
Implicit-Explicit Runge-Kutta integration
(HEVI)

Implicit-Explicit scheme in the MCV framework

For example,
Backward Euler(BE)

$$\frac{q^{n+1} - q^n}{\Delta t} = \mathcal{L}(q^n) + J(q^{n+1} - q^n)$$

Linear algebraic equations:
iterative or *LU solver*

$$J = \frac{\partial \mathcal{L}(q)}{\partial q}$$

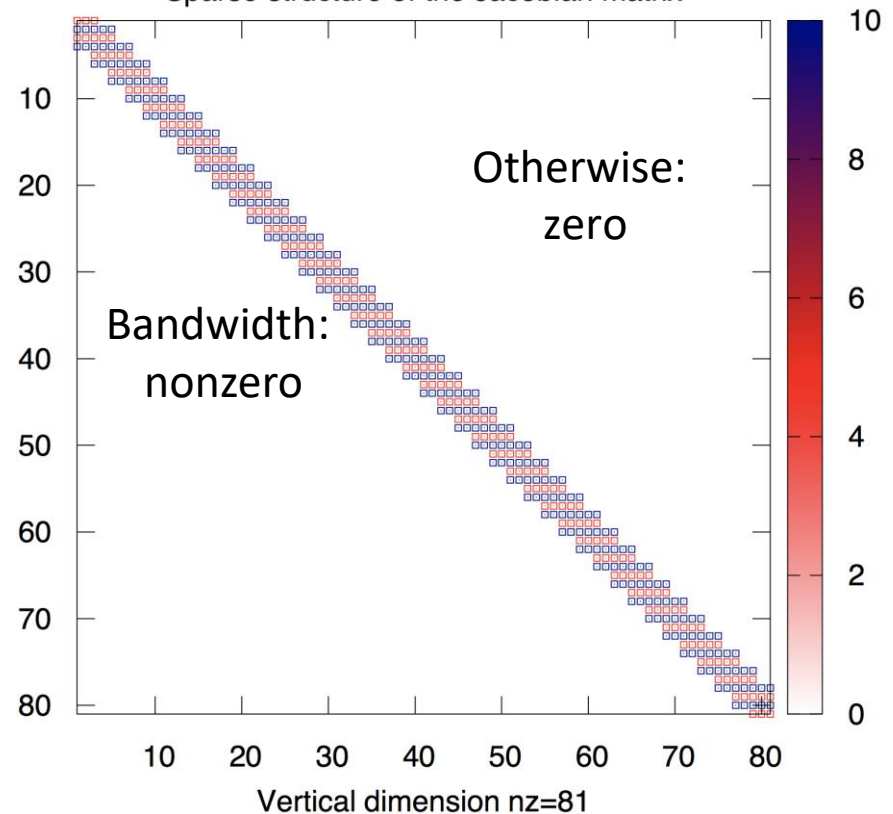
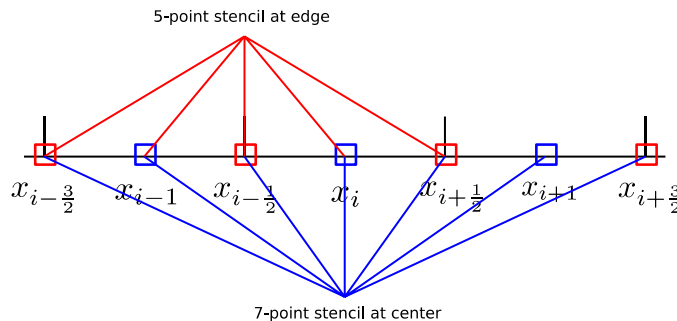
Local linearization

$$Ax = B \iff (\Delta t I + J)(q^{n+1} - q^n) = \mathcal{L}(q^n)$$

Sparse structure of the Jacobian matrix

Structure of Jacobian matrix

J



Implicit-Explicit scheme in the MCV framework

For example,

Backward Euler(BE)

$$\frac{q^{n+1} - q^n}{\Delta t} = \mathcal{L}(q^n) + J(q^{n+1} - q^n)$$

*Linear algebraic equations:
iterative or LU solver*

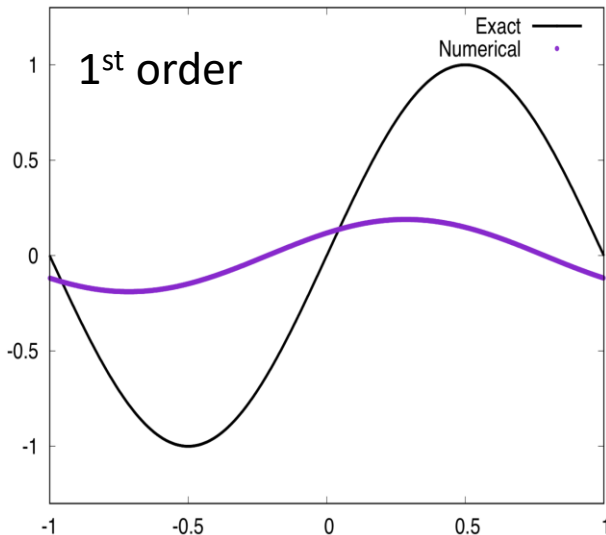
$$J = \frac{\partial \mathcal{L}(q)}{\partial q}$$

Local linearization

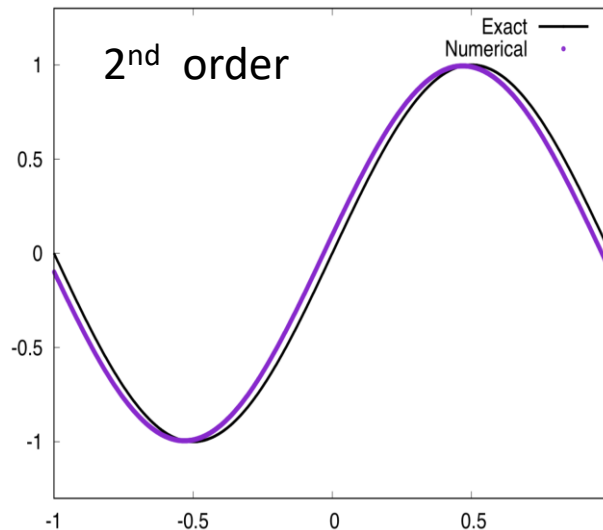
CFL=100

$$Ax = B \iff (\Delta t I + J)(q^{n+1} - q^n) = \mathcal{L}(q^n)$$

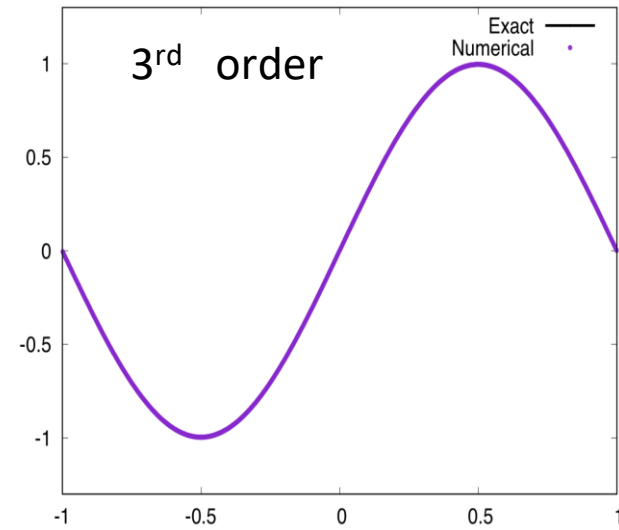
Backward Euler (BE)



Crank-Nicolson(CN)



Implicit RK3(imRK3)



Advection test

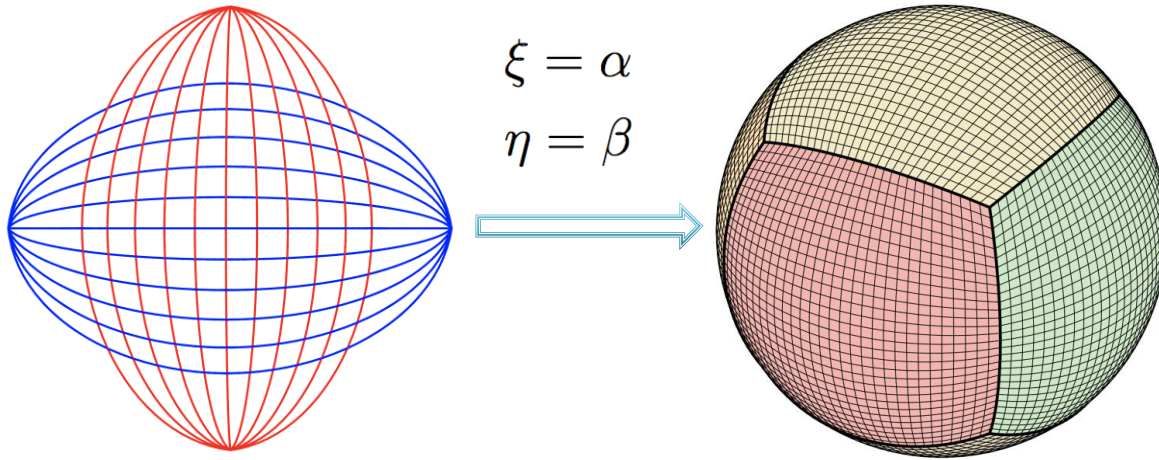
Numerical results – purple solid lines True solution – black solid lines

■ **Nonhydrostatic MMFV-Core on the cubed-sphere**

Summary of MMFV DynCore features

Model aspect	MMFV DynCore
Equation system	fully compressible flux-form
Prognostic variables	$(\rho'_d, u^\xi, u^\eta, w, (\rho_d \theta)', r_X)$
Horizontal discretization	structured MMFV(3 rd or 4 th)
Vertical discretization	structured MMFV(3 rd or 4 th)
Time-stepping scheme	3 rd RK-IMEX (HEVI)
Horizontal grid	cubed sphere
Horizontal coordinates	$(\alpha, \beta) \in [-\pi/4, \pi/4]$
Vertical coordinate	generalized height-based terrain following
Horizontal staggering	co-located
Vertical staggering	co-located
Advection	conservative MCV3+WENO/BGS+PRM/CSLR+FCT

The gnomonic Cubed-Sphere



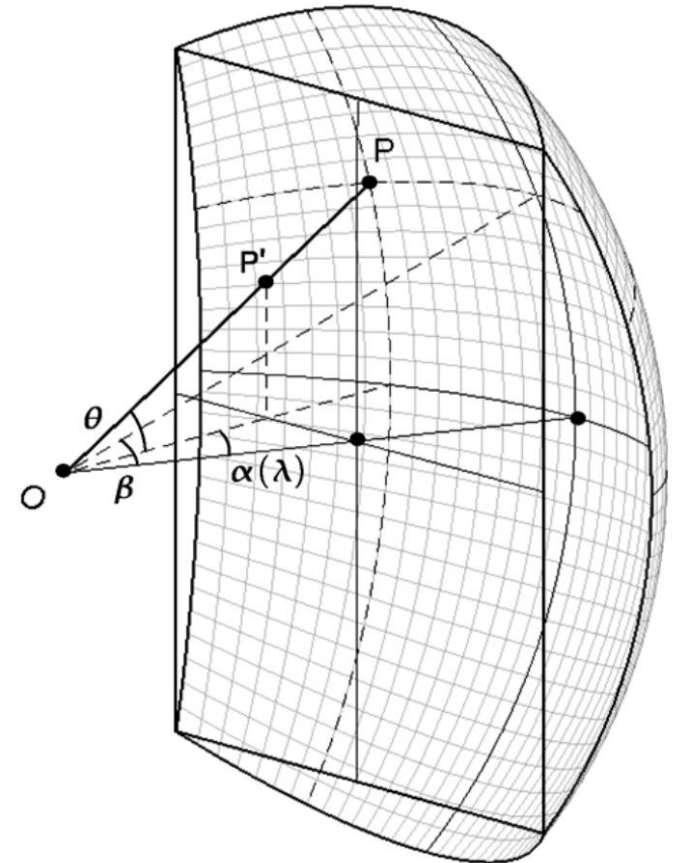
Equiangular center projection

$$(\alpha, \beta) \in \left[-\frac{\pi}{4}, \frac{\pi}{4}\right] \times \left[-\frac{\pi}{4}, \frac{\pi}{4}\right]$$

The coordinate line on the boundary is broken. The ghost cells are used to exchange the data in the neighboring patches.

(1) For scalar variables, the numerical average is adopted

(2) For vector variables, the directional numerical averaging should be considered.



The flux-form governing Eqs on curvilinear system

$$\frac{\partial \mathbf{q}}{\partial t} + \frac{\partial \mathbf{e}(\mathbf{q})}{\partial \xi} + \frac{\partial \mathbf{f}(\mathbf{q})}{\partial \eta} + \frac{\partial \mathbf{h}(\mathbf{q})}{\partial \zeta} = \mathbf{s}_m + \mathbf{s}_c + \mathbf{s}_g + \mathbf{s}_r$$

Thermodynamic splitting:

$$\left\{ \begin{array}{l} \rho(\mathbf{x}, t) = \bar{\rho}(\mathbf{x}) + \rho'(\mathbf{x}, t) \\ p(\mathbf{x}, t) = \bar{p}(\mathbf{x}) + p'(\mathbf{x}, t) \\ (\rho\theta)(\mathbf{x}, t) = \overline{(\rho\theta)}(\mathbf{x}) + (\rho\theta)'(\mathbf{x}, t) \end{array} \right.$$

Prognostic variables: $\mathbf{q} = (\sqrt{G}\rho', \sqrt{G}\rho u^\xi, \sqrt{G}u^\eta, \sqrt{G}\rho w, \sqrt{G}(\rho\theta)')^T$

Annotations for the governing equation:

- Coriolis force** (points to \mathbf{s}_c)
- Vertical non-reflection boundary** (points to \mathbf{s}_r)
- Curvilinear system geometry** (points to \mathbf{s}_m)
- Gravity** (points to \mathbf{s}_g)

ξ and η are the local coordinates on the curvilinear system.

$\zeta = \zeta(\xi, \eta, z)$ is the height-based terrain following coordinate

$\sqrt{G} = \sqrt{G_c}\sqrt{G_v}$ is the composite Jacobian of transformation

HEVI time integration of MM-FV DynCore

$$\frac{\partial \mathbf{q}}{\partial t} + \boxed{\frac{\partial e(\mathbf{q})}{\partial \xi} + \frac{\partial f(\mathbf{q})}{\partial \eta}} + \boxed{\frac{\partial h(\mathbf{q})}{\partial \zeta}} = \boxed{\mathbf{s}_m + \mathbf{s}_c} + \boxed{\mathbf{s}_g + \mathbf{s}_r}$$

Non-stiff terms: Explicit computation

Stiff terms: implicit computation

Spatial discretization: MCV3/MCV3-4th scheme

IMEXRK time marching:

3rd order IMEXRK

(Cavaglieri & Bewley JCP, 2015;
Weller et al., JCP, 2013)

$$\begin{aligned} \mathbf{q}^{(j)} &= \mathbf{q}^{(n)} + \boxed{\Delta t \sum_{\ell=1}^{j-1} a_{j\ell} \mathcal{H}(\mathbf{q}^{(\ell)}, t^n + c_\ell \Delta t)} + \boxed{\Delta t \sum_{\ell=1}^{j-1} \tilde{a}_{j\ell} \mathcal{V}(\mathbf{q}^{(\ell)}, t^n + \tilde{c}_\ell \Delta t)} + \boxed{\Delta t \tilde{a}_{jj} \mathcal{V}(\mathbf{q}^{(j)})} \\ \mathbf{q}^{n+1} &= \mathbf{q}^{(n)} + \Delta t \sum_{j=1}^{\mu} w_j \mathcal{H}(\mathbf{q}^{(j)}, t^n + c_j \Delta t) + \Delta t \sum_{j=1}^{\mu} \tilde{w}_j \mathcal{V}(\mathbf{q}^{(j)}, t^n + \tilde{c}_j \Delta t) \quad j = 1, \mu \end{aligned}$$

\mathcal{H} : Non-stiff \mathcal{V} : stiff

- The time step is limited by stability condition of horizontal explicit computation (CFL \approx 0.8 for MCV3-4th scheme (Chen & Xiao, JCP, 2008)).
- HEVI time integration is conducted by 3-stage RK-IMEX scheme and has 3rd order accuracy in time.
- Nonlinear terms are solved by using Newton's iteration and linear algebraic equation is presently solved by utilizing LINPACK (direct method).

3D benchmark results

■ Non-hydrostatic MM-FV DynCore

- ✓ 3D Rising thermal bubble
- Cartesian ✓ 3D nonhydrostatic mountain wave
- ✓ 2D moist bubble/thunder storm
- ✓ 3D Rossby-Haurwitz wave
- ✓ 3D mountain-Rossby wave
- Cubed sphere ✓ 3D gravity wave
- ✓ 3D baroclinic wave
- ✓ Schär-type Mountain on reduced-size planet
- ✓ Held–Suarez climatology
- ✓

Details of some tests on sphere are referred to

C. Jablonowski et al., Idealized test cases for the dynamical cores of atmospheric general circulation models: a proposal for the NCAR ASP 2008 summer colloquium, Tech. rep. (2008)

Paul A. Ullrich et al., Dynamical Core Model Intercomparison Project (DCMIP) Test Case Document DCMIP summer school (2012)

Simulation of Strongly stratified flow past a steep isolated hill

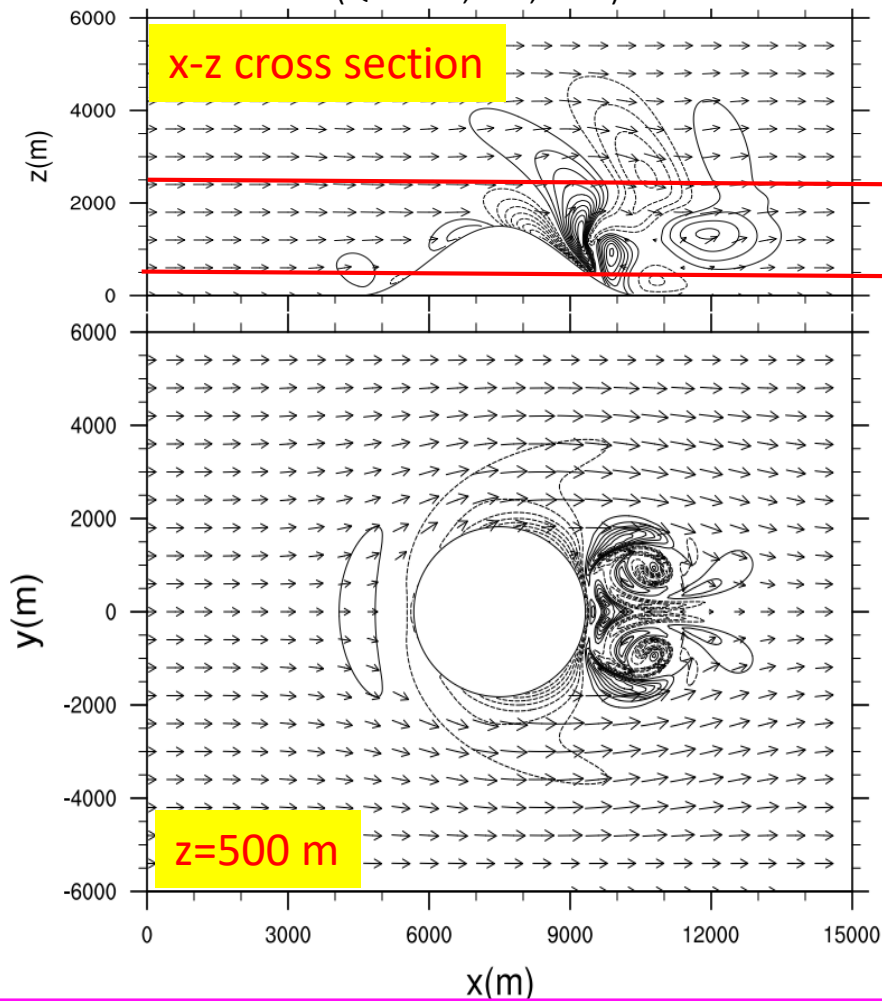
$$h(x, y) = h_0 \cos^2(\pi r/2L) \text{ if } r = ((x - x_0)^2 + (y - y_0)^2)^{1/2} \leq L \quad (\text{No rotation: } f = 0)$$

Froude number is 1/3

$h(x, y) = 0$ otherwise, where the half-width $L = 3000$ m and height $h_0 = 1500$ m

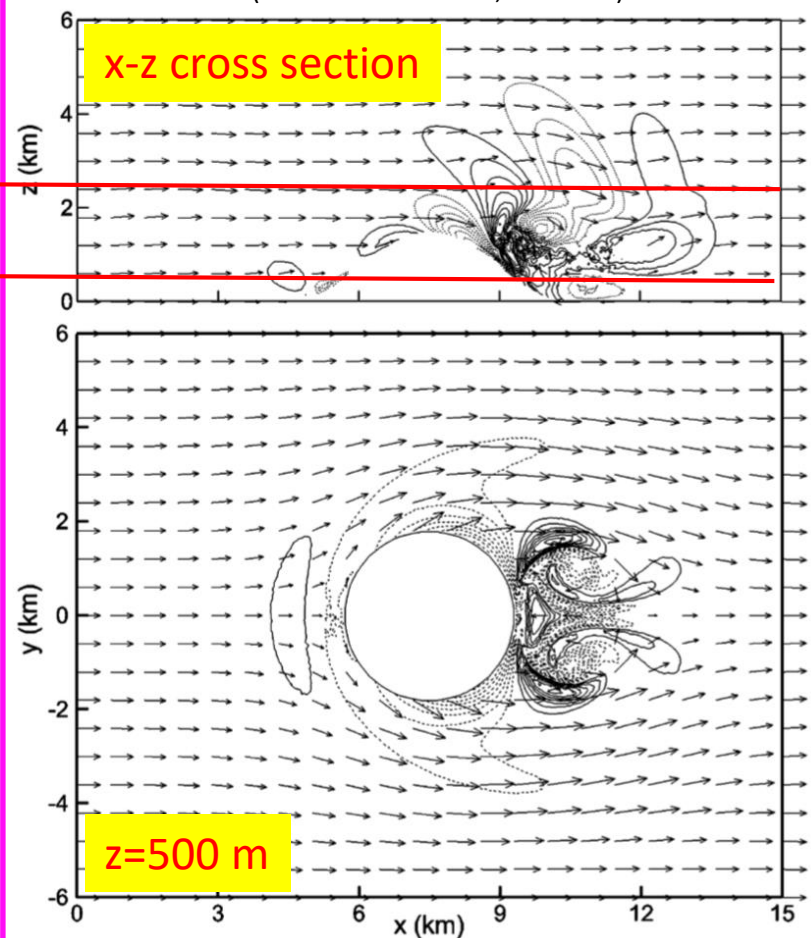
MCV3 nonhydrostatic DynCore

(Qin et al., AAS, 2019)



ECMWF FV nonhydrostatic module

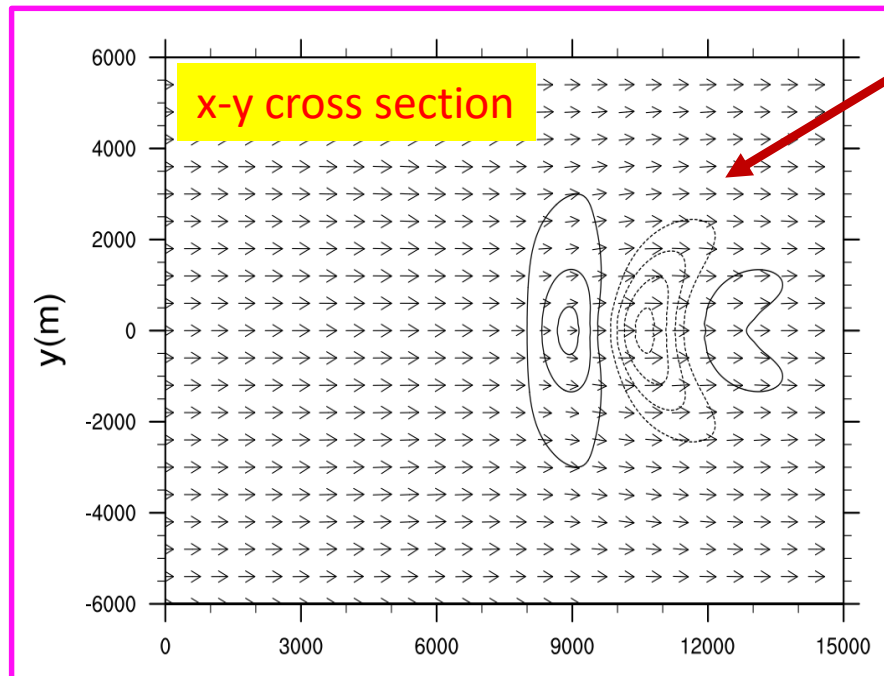
(Smolarkiewicz et al., JCP 2016)



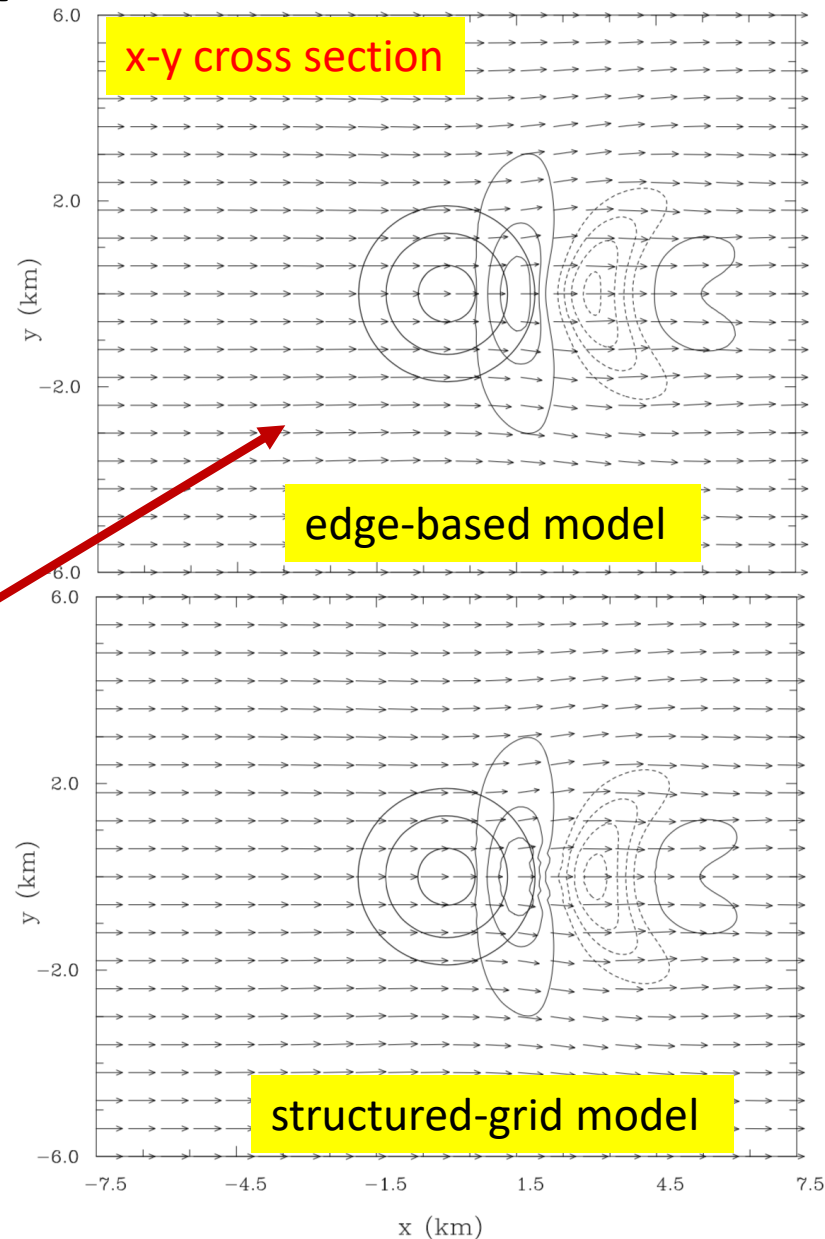
Simulation of Strongly stratified flow past a steep isolated hill

Vertical velocity at $z=2500$ m

MCV3 nonhydrostatic DynCore
(Qin et al., AAS, 2019)



ECMWF FV nonhydrostatic module
(Smolarkiewicz et al., JCP 2016)

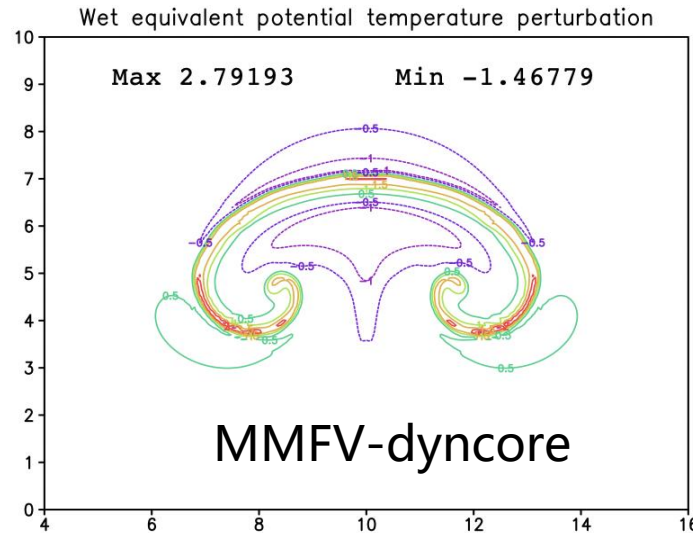


Testcase: moist atmospheric dynamics

Test case: 2D moist rising bubble

Bubble top: about 7km

$$\Delta x = \Delta z = 100 \text{ m}$$



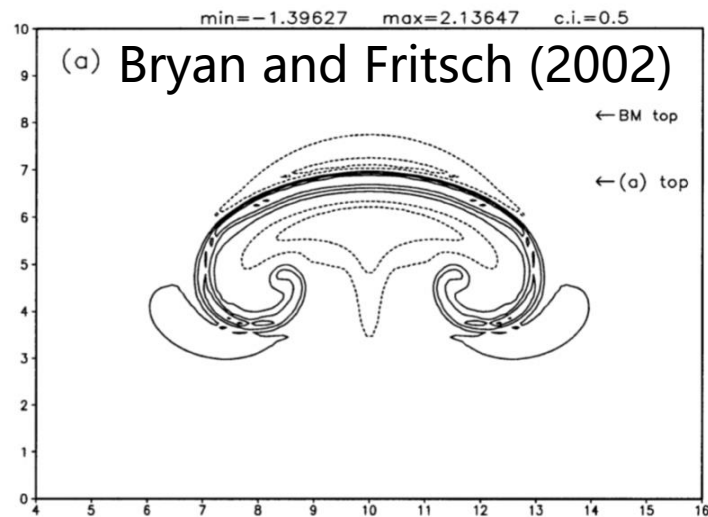
(a)

See Table 1

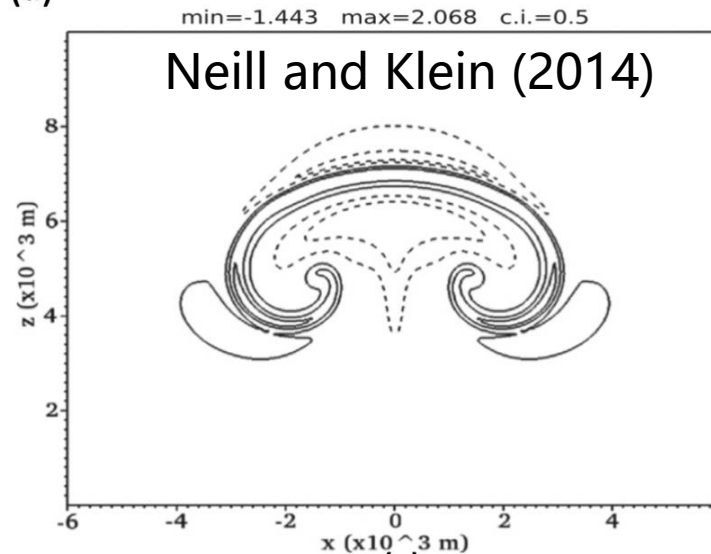
(Bryan and Fritsch, 2002)

set A

$$\frac{D \ln \theta}{Dt} = \frac{L_v \dot{q}}{c_p T}$$



(b)



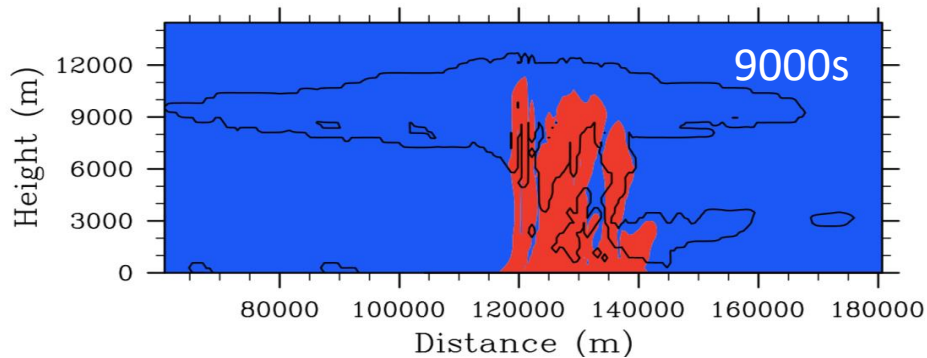
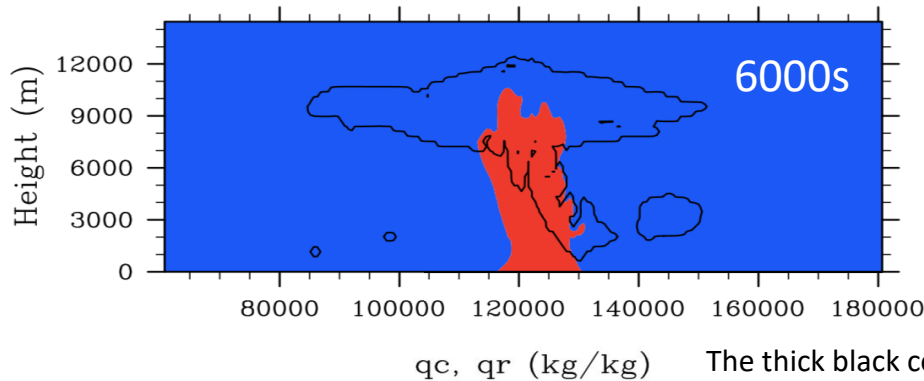
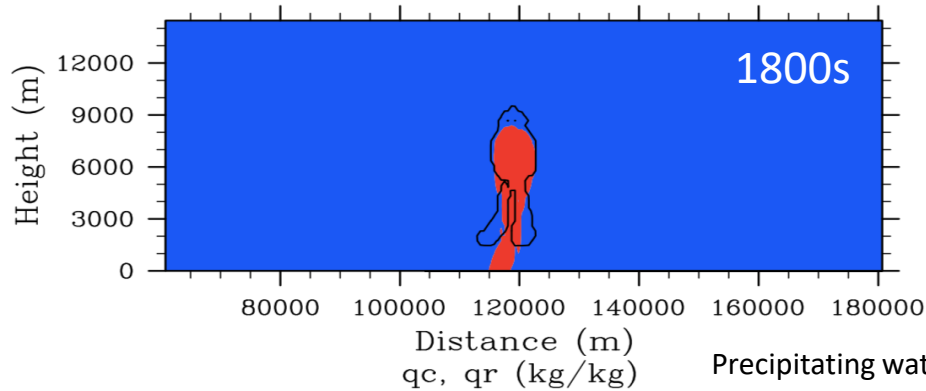
(c)

Test case: 2D thunder storm

FE-VMS model

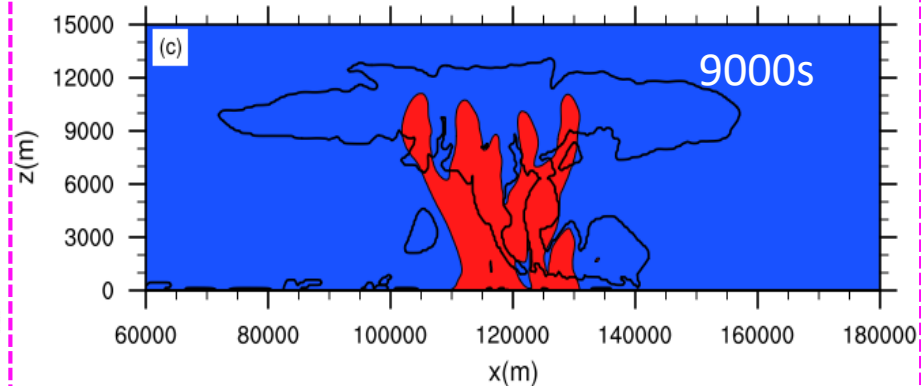
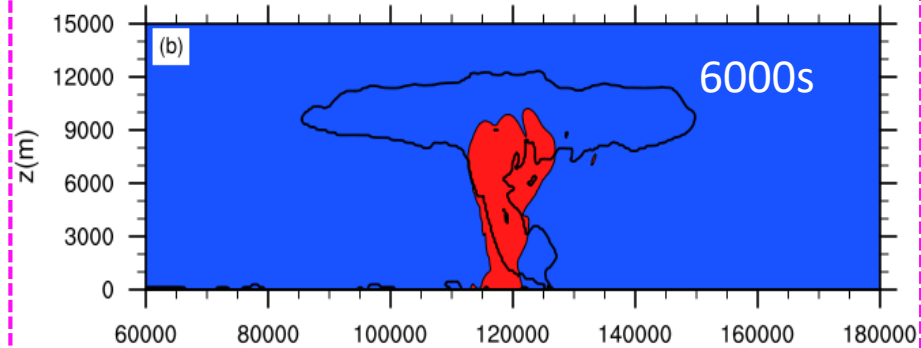
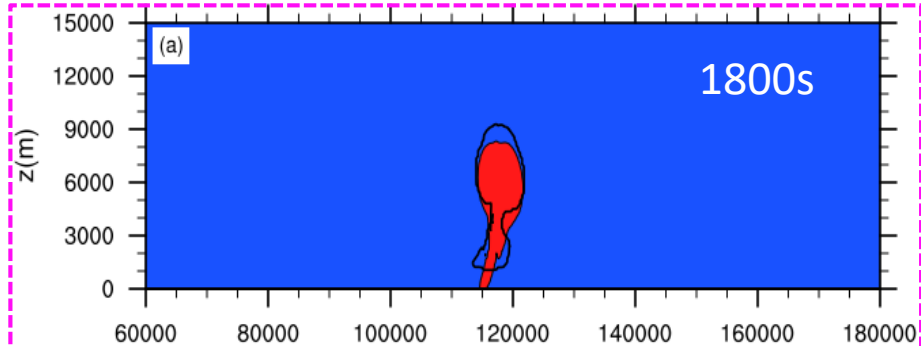
Kessler-type parameterization

q_c, q_r (kg/kg) (Marras et al., JCP, 2013)



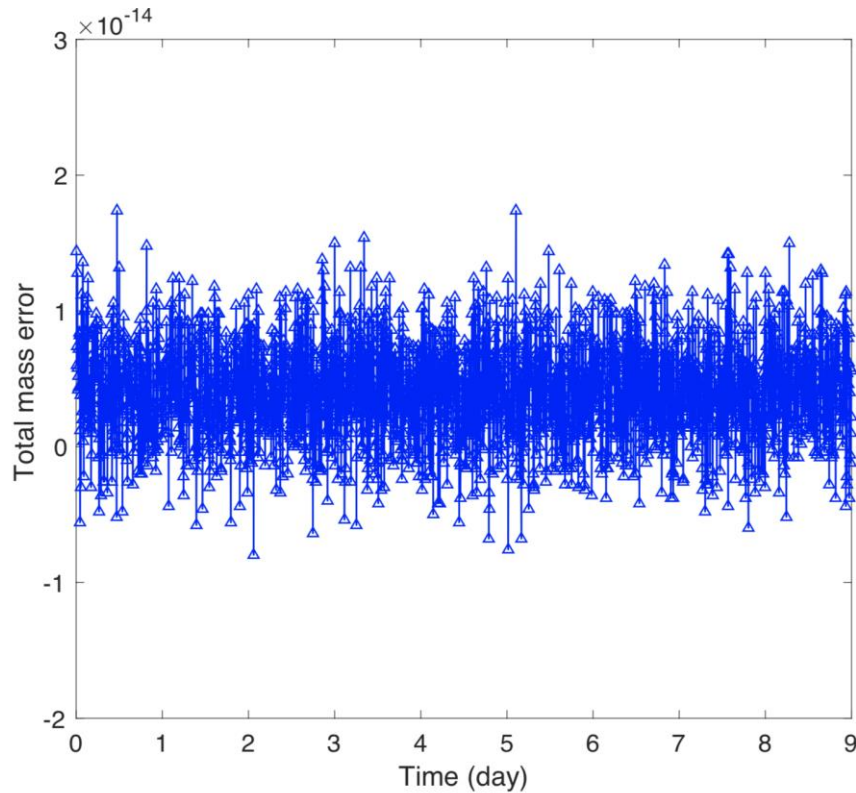
MMFV model

q_c, q_r (kg/kg)

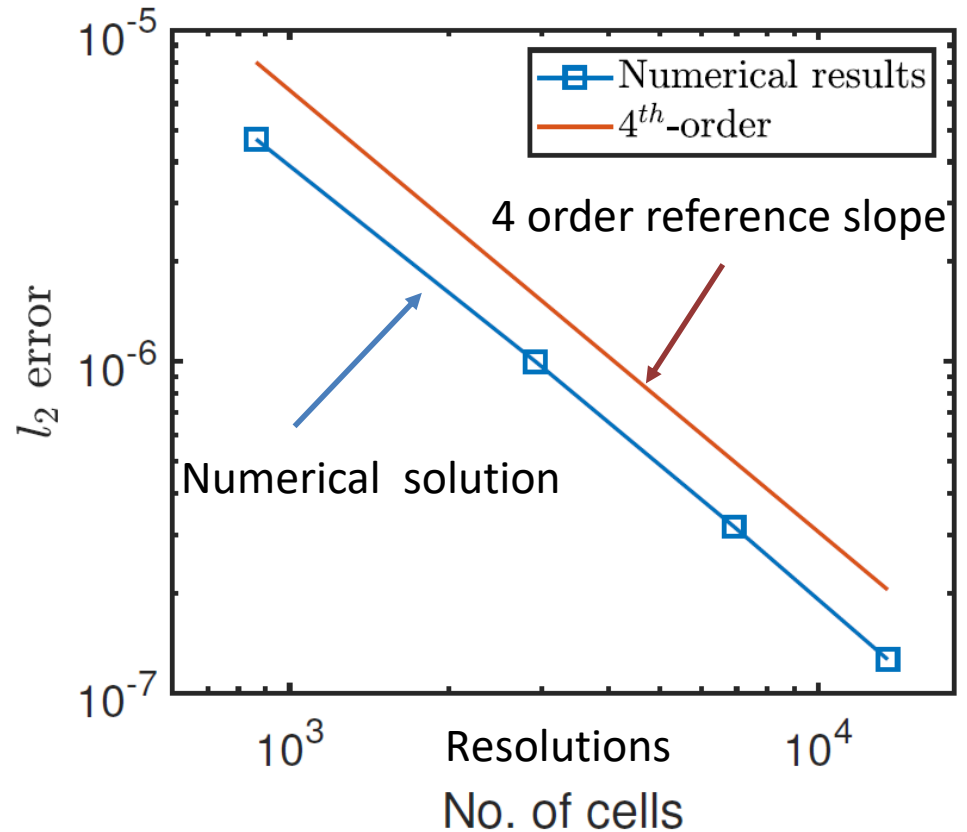


High-order nonhydrostatic 3D MMFV DynCore

Relative mass errors



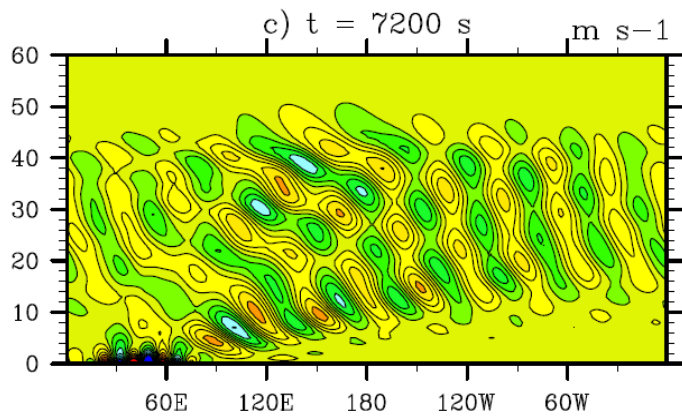
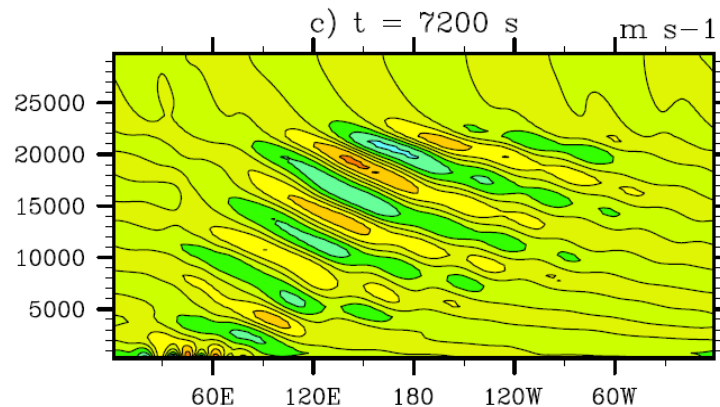
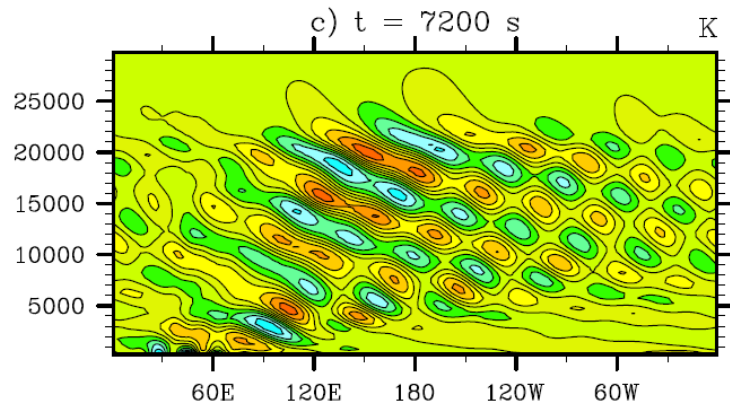
4th order convergence



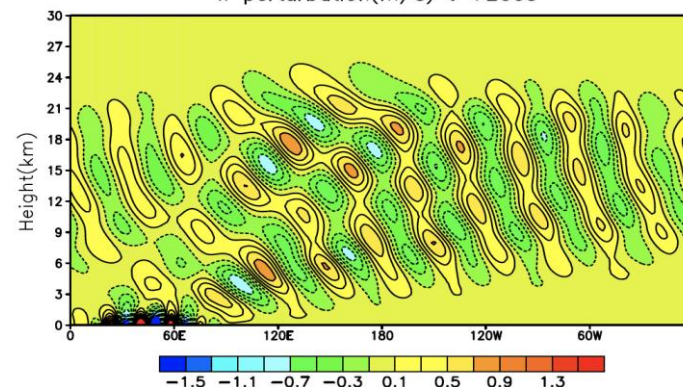
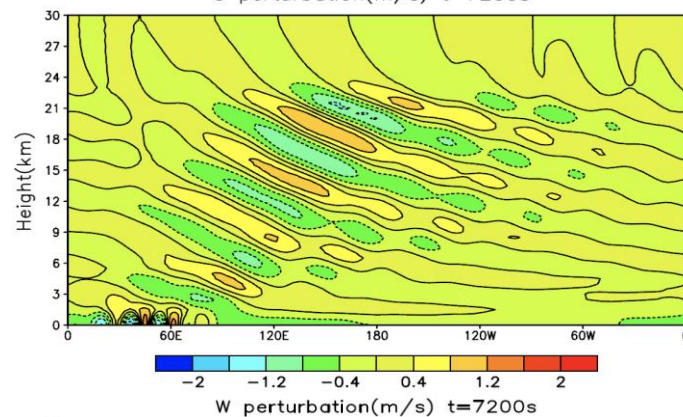
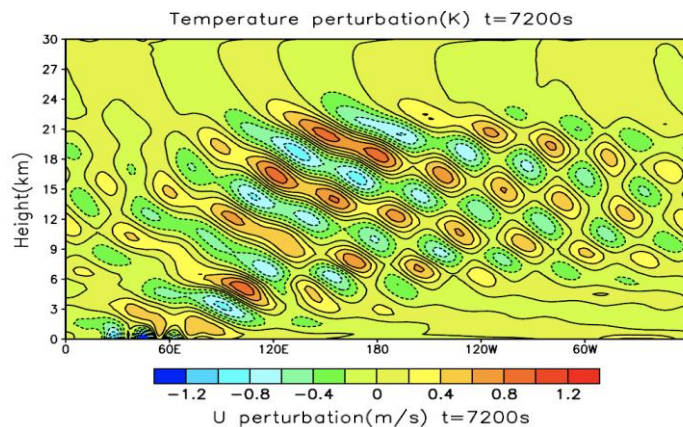
Benchmark: Schär mountain wave on small planet

(Ullrich et al., DCMIP-2012:Test 2-1; Klemp et al., 2015, JAMES)

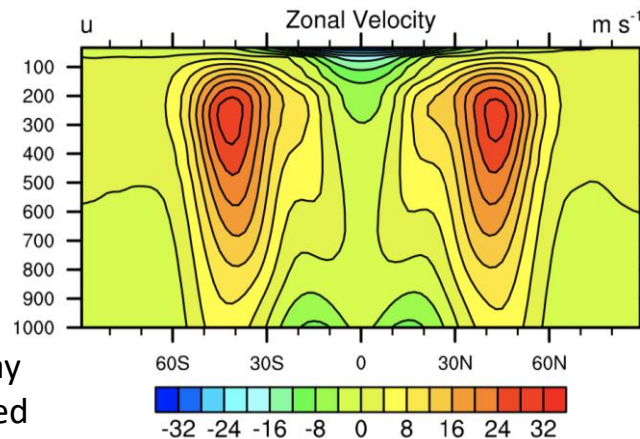
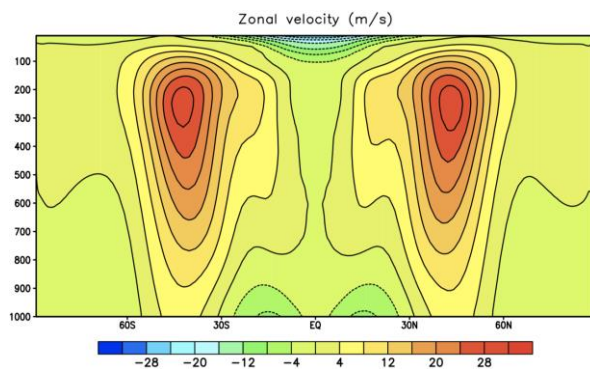
EndGame



MMFV

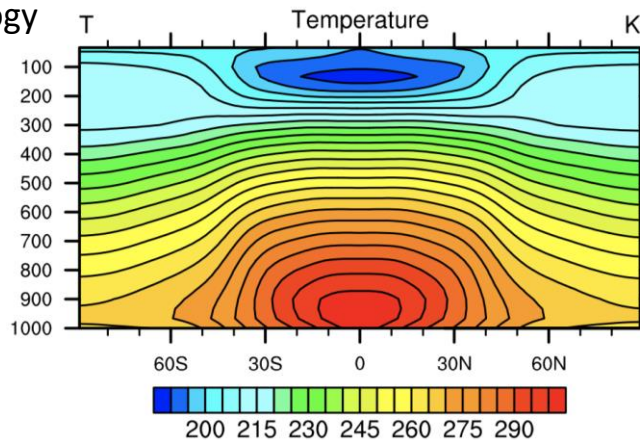
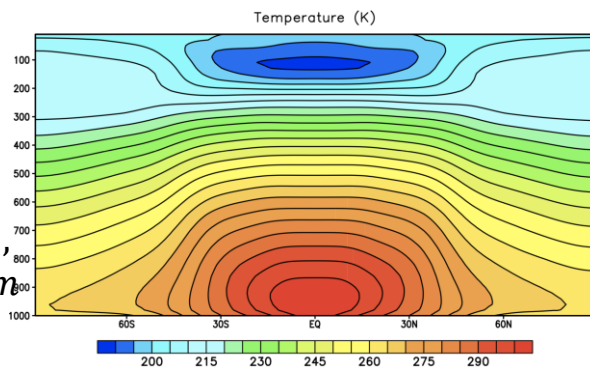


Benchmark: Held-Surez climatology (preliminary results)



MMFV
DynCore

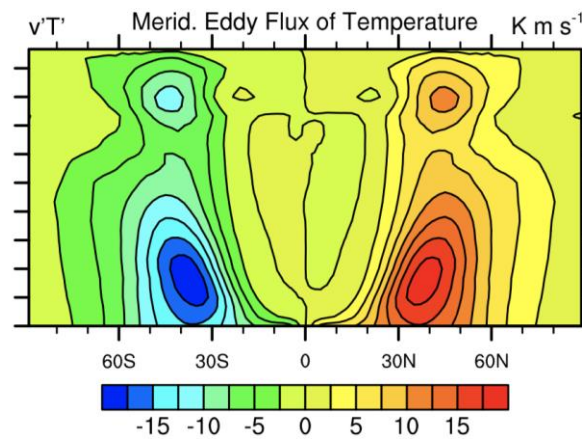
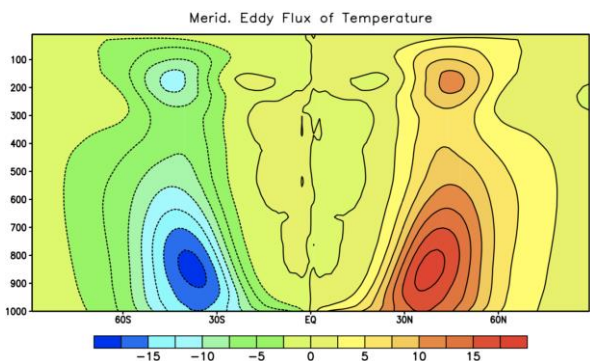
$\Delta_{DOF} \approx 1.875^\circ$,
41 levels, 30km



MCore

(Ullrich & Jablonowski, JCP, 2012)

$\Delta_{DOF} \approx 1.875^\circ$,
30 levels, 30km

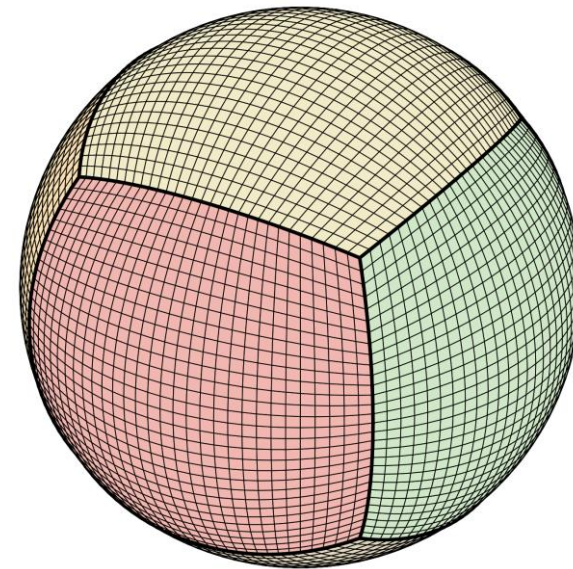


MMFV CPU+MIC hybrid parallel acceleration and scalability

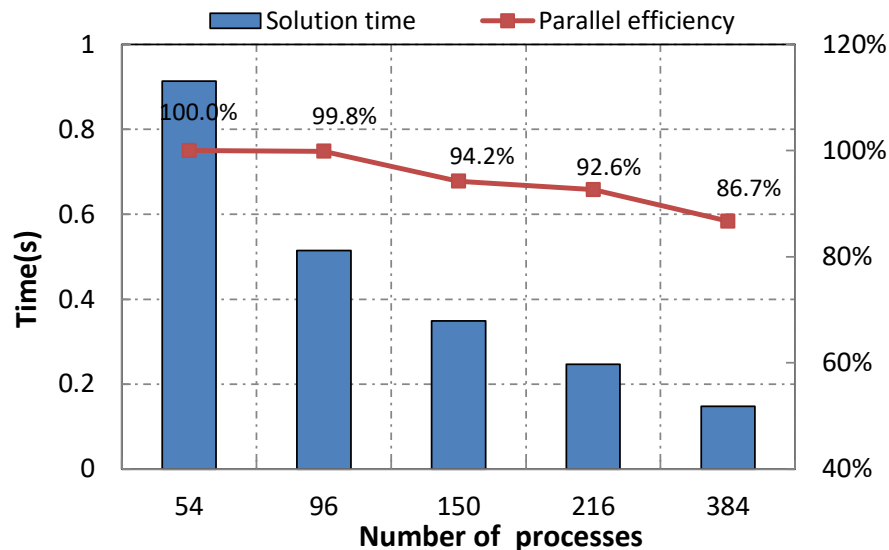
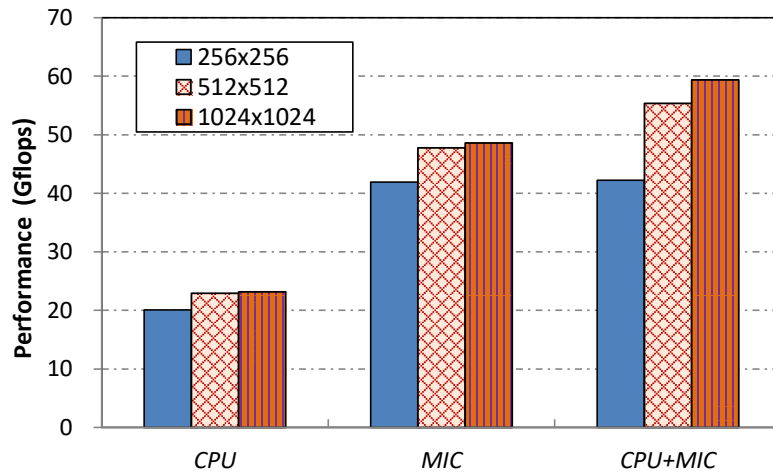
(Zhang et al., 2017, J. Supercomput.)

(Based on cubed sphere shallow water model)

CPU+MIC hybrid parallel speedup is 2.56 in compared with CPU version



Scalable from 54 processes (3726 cores) to 384 processes (26496 cores) and paralleling efficiency is 86.7%.



Summary

- The novel multi-moment finite volume method has the good numerical properties such as high order, conservation, scalability, grid-robustness, large CFL in comparison with other high-order scheme like DG.
- The limiting projection like WENO and BGS scheme has been designed based on the multi-moment finite volume framework. The positive-definite technique of MMFV scheme is developed as well.
- The SWE and 2D nonhydrostatic model are verified by many benchmarks.
- The MM-FV DynCore on cubed sphere has been developed, which is well-balanced among solution quality (accuracy and robustness), algorithmic simplicity, computational efficiency and flexibility.
- The MMFV DynCore has been validated through ideal tests, which indicates that the MM-FV DynCore is very promising for NWP and even climate simulations.
- Under the way: real Physic-Dynamic coupling , more test cases and evaluation of parallel acceleration and scalability of MM-FV DynCore, ...

Thanks for your attention!
Question?

